International Journal of Fatigue 209 (2026) 109627

Contents lists available at ScienceDirect

International Journal of Fatigue

journal homepage: www.elsevier.com/locate/ijfatigue

Discontinuity-controlled fatigue performance and model assessment for LPBF-M789 maraging stainless steel with different surface conditions

K. Sanni [a,*], A. D'Andrea [b], M. Cova [c], L. Patriarca [d], M. Brochu [a]

[a] Department of Mechanical Engineering, Polytechnique Montreal, 2500 ch. De Polytechnique, Montreal H3T 1J4, Canada
[b] Department of Mechanical Engineering, École de Technologie Supérieure, 1100 Notre-Dame Street W, Montreal, Quebec H3C 1K3, Canada
[c] SACMI S.C. Via Provincial Selice 17/A, Imola 40026, Bologna, Italy
[d] Department of Mechanical Engineering, Politecnico di Milano, Milano, Italy

ARTICLE INFO

Keywords:
M789 alloy
Discontinuity
KT diagram
Cracks
Pits
Murakmi
El-Haddad

ABSTRACT

Laser Powder Bed Fusion (LPBF) M789 is a recently developed alloy for fatigue-critical tooling applications, yet its fatigue behaviour in the presence of intrinsic and extrinsic discontinuities remains largely uncharacterised. This study evaluates the discontinuity-controlled fatigue response of the alloy using polished, as-printed, and corrosion-pitted specimens, fatigue tested and complemented by non-destructive characterisation, fractography, and extreme value analysis. A Kitagawa–Takahashi diagram incorporating the experimentally measured long-crack threshold was employed to assess the applicability of LEFM, El-Haddad, and Murakami models. The experiments highlighted that failure initiated at discontinuities with contributions from the microstructure. Fatigue strength ranged from 93 to 282 MPa depending on surface condition, making the idealised peak fatigue strength unattainable. Process-induced discontinuities exhibited crack-like behaviour accurately captured by LEFM and El-Haddad models, whereas corrosion pits have a notch-controlled behaviour driven by geometry, with minimal interaction effect between neighbouring discontinuities. The geometric effects account for deviations from fatigue-strength predictions and demonstrate that discontinuity size alone is insufficient to rank severity when morphologies differ. Overall, the study establishes a discontinuity-informed basis for predicting the fatigue behaviour of LPBF M789 and supports the development of reliable design methodologies for fatigue-critical tooling components manufactured from the alloy.

1. Introduction

Additive manufacturing (AM) has become a mainstay technology in the manufacturing industry, with laser powder bed fusion (LPBF) spearheading its popularity. LPBF's patronage stems from its versatility in processing a wide range of materials, dimensional accuracy, and part reproducibility. Thus, industries such as aerospace, biomedical and automotive find the LPBF an attractive option for parts with interesting strength-to-weight ratio [1].

Despite its advantages, LPBF-produced parts often contain discontinuities such as lack of fusion (LOF), non-metallic inclusions (NMI), gas pores, and surface roughness in the as-printed condition. These challenges are continually addressed through improved process control and post-processing treatments, resulting in parts with enhanced integrity. Additionally, extrinsic discontinuities such as corrosion-induced pits are being mitigated through better mechanical design and material selection. As a result, the mechanical properties of LPBF materials are becoming more consistent, with progress being made in enhancing their fatigue resistance. In the critical review of Kan et al. [2] on processed induced porosity in LPBF alloys, they identified Ti-6Al-4 V, Inconel 718, AISI 316 L and AlSi10Mg as the most commonly investigated LPBF alloys. However, recent research trends have shown that there is an increasing interest in LPBF tool steels like the H13 and M2 alloys [3].

In the context of fatigue, discontinuities in LPBF alloys negatively impair their resistance. This fatigue debit is attributed to stress localisation, crack initiation and propagation to failure of the part. Several authors have identified size as a key influencer of the severity of a discontinuity on fatigue strength [4–6]. However, other considerations, like the shape and location of the discontinuity, contribute to its severity. According to Nadot [7], five critical factors that influence the severity are: i) size, ii) type, iii) position, iv) morphology, and v) loading conditions. Furthermore, the rough surface of as-printed LPBF parts contributes to stress concentration, either acting singularly as troughs or

* Corresponding author.
E-mail address: kashim.sanni@etud.polymtl.ca (K. Sanni).

https://doi.org/10.1016/j.ijfatigue.2026.109627
Received 20 December 2025; Received in revised form 24 February 2026; Accepted 9 March 2026
Available online 14 March 2026

Nomenclature

AM	Additive manufacturing
BD	Building direction
CDF	Cumulative distribution function
CE	Counter electrode
EDS	Energy dispersive X-ray spectroscopy
EVS	Extreme value statistics
FA	Fatigue as-printed specimens
FC	Fatigue-pitted specimens
FEA	Finite element analysis
FP	Fatigue polished specimens
HV	Vickers hardness
KTD	Kitagawa Takahashi diagram
LC	Long cracks
LD	Loading direction
LEFM	Linear elastic fracture mechanics
LOF	Lack of fusion
LPBF	Laser powder bed fusion
NA	Not available
ND	Natural discontinuities
NDC	Non–destructive characterisation
NMI	Non-metallic inclusion
PAGB	Parent austenite grain boundary
PAGS	Parent austenite grain size
PD	Printing direction
PDF	Probability density function
PFS	Peak fatigue strength
PH	Precipitation hardened
RE	Reference electrode
SCF	Stress concentration factor
SEB	Single edge bending
SEM	Scanning electron microscope
SI	Supplementary information
SL	Sample length
S-N	Stress versus number of cycles
WE	Working electrode

List of symbols

σ_a	stress amplitude
σ_{FS}	fatigue strength in the presence of discontinuities
$\sigma_{w,0}$	fatigue strength of discontinuity-free material for a stress ratio of −1
$\sigma_{w,0.1}$	fatigue strength of discontinuity-free material for a stress ratio of 0.1
$\sigma_{w,Nlife}$	computed fatigue strength at N_{life} cycles
$\Delta\sigma$	stress range
α	material parameter
$\sqrt{area}$	projected area of discontinuity perpendicular to the loading direction
$\Delta K_{I,max}$	maximum stress intensity range ahead of an arbitrary crack front
$\Delta K_{th,LC}$	stress intensity range threshold for long cracks
$\Delta K_{th,sc}$	stress intensity range threshold for short cracks
A_{ref}	reference area
A_0	inspection area
K	stress intensity factor
k_t	stress concentration factor
N_{life}	number of cycles of interest
P	load
R	stress ratio
$R_{v,max}$	maximum value of the depth of a trough on a roughness profile
S_u	tensile strength
T	return period
V_{ref}	reference volume
V_0	inspection volume
Y	geometric factor
a	crack dimension
a_0	El-Haddad characteristic crack length
c	depth of trough

in combination with other discontinuities. As such, there is a competitive quest amongst these influencing factors to drive part failure.

The typical cellular microstructures, melt pool boundaries and characteristic texturing that characterise LPBF alloy also influences their mechanical properties [8]. This influence often manifests in densely built LPBF parts with low porosity, finely polished surface, and microstructural features comparable to the discontinuity sizes. Kan et al. [2] have also identified build quality and finishing as important in determining whether failure is driven by discontinuity or microstructure. In an earlier work, Nadot et al. [9] showed that there exists a competition for failure trigger between the microstructure and discontinuity size for identical specimen geometry, loading conditions, and discontinuity morphology. They concluded that the relative size of a discontinuity, in comparison to the characteristic microstructural dimension, was more critical to fatigue strength. These findings exemplify the role of the microstructure on fatigue failure, notwithstanding the presence of discontinuities.

In many service applications, components produced by LPBF are required to perform under cyclic loading conditions for a specified number of cycles. Typically, these requirements correspond to high-cycle fatigue regimes, i.e. 10^6 or 10^7 loading cycles. A common design tool used to assess the fatigue resistance of material containing discontinuities is the Kitagawa-Takahashi (KT) diagram proposed in 1976. The diagram depicts the relationship between the size of discontinuities and fatigue strength [10]. Originally, their work set out to investigate the applicability of fracture mechanics to short cracks and, in the course, observed the existence of a transition zone from short to long cracks. Consequently, the authors unveiled the evolution of the fatigue strength with the increasing size of discontinuities. Several models, like El–Haddad [11] and Murakami [12] (discussed briefly in section 2), have been further proposed to improve the modelling accuracy of the trend of the KT diagram, and enhance conservatism. Today, researchers often leverage the KT diagram to understand the influence of discontinuities on the fatigue behaviour of LPBF alloys. Wu et al. [13] employed the KT diagram to study the anisotropic fatigue resistance of LPBF-produced AlSi10Mg alloys by shedding light on the orientation of discontinuity, relative to the build direction. In another application, Cersullo et al. [14] predicted fatigue life by incorporating local stress and size of discontinuity into the KT diagram. More recently, Bergant et al. [15] employed the KT diagram in exploring the significance of discontinuities on the behaviour of electron beam melted Ti-6Al-4 V alloy. These examples, to mention but a few, underscore the versatility of the KT diagram in studying the fatigue behaviour of materials dominated by discontinuities.

Given the sensitivity of fatigue strength to discontinuities, it becomes essential to understand their influence on newly developed LPBF alloys intended for cyclic loading applications. Recently, Böhler pioneered a maraging stainless steel called M789 [16] engineered to combine the strength of maraging steels and the corrosion resistance of precipitation hardened (PH) steels [16]. The alloy is intended for use as a tooling material for die inserts in a high cycle loading application, requiring static and cyclic strength and good corrosion resistance.

Recent research conducted on the alloy focused more on its microstructural properties and very little on its mechanical properties. For instance, Tian et al. [17] investigated the microstructure and static mechanical properties of the M789 LPBF alloy in as-printed and age-hardened conditions. They described the microstructure as having a random crystallographic texture and mechanical properties that are comparable in both the building and transverse directions. In another work [18], the same authors focused on the effect of age-hardening heat treatment on the alloy and reported the presence of plate-like and spherical Al and Ni-rich precipitates in the microstructure. As of late, Ordnung et al. [19] showed that the use of an incremental dual LPBF process can markedly enhance the fatigue performance of the M789 alloy by reducing surface roughness, lowering stress concentration and removing subsurface pores. Their fatigue findings were focused on the global fatigue performance of the alloy across different numbers of cycles and not on the discontinuity influence. In a rather different approach, Laliberté–Riverin et al. [20] conducted a preliminary investigation into the alloy's discontinuities and corrosion properties, and employed theoretically estimated parameters to construct its KT diagram. Although Laliberté–Riverin et al.'s [20] work provided valuable insights on the discontinuity influence, further information is desired on the alloy's fatigue behaviour. Particularly, the influence of as-printed surfaces and extrinsic discontinuities like corrosion pits, not characterised in their work. Additionally, for a reliable KT diagram, Schönbauer and Mayer [21] recommend experimentally obtaining the stress intensity range threshold for long cracks, $\Delta K_{th,LC}$. The work of Laliberté–Riverin et al. [20] used a theoretical estimate of $\Delta K_{th,LC}$ of 4.42 MPa $\sqrt{m}$ for the KT diagram of the alloy, but a full evaluation of $\Delta K_{th,LC}$ is still pending. A comparison of S-N data of the M789 with alloys in the same class such as the 18Ni300 maraging steel, 17–4 PH steel and 316 L stainless steel is presented in Fig. 1. The fatigue performance of the alloy falls within the same range as other additively manufactured steels such as LPBF 18Ni300 maraging steel, LPBF 316 L stainless steel, and LPBF 17–4 PH stainless steel, with differences likely influenced by discontinuity population rather than microstructure. While this trend is apparent, it triggers a need to explore the discontinuity influence associated with the more recent M789 alloy. A quick search at the time of this work on the Web of Science returned just the two articles of Ordnung et al. [19] and Laliberté–Riverin et al. [20] on fatigue of the M789 alloy. Therefore, the fatigue behaviour of the alloy remains insufficiently understood, particularly regarding discontinuity-controlled fatigue mechanisms and their representation within the Kitagawa-Takahashi framework. This limitation hinders reliable fatigue design and qualification of M789 components intended for cyclic loading applications.

The present study addresses the knowledge gap by investigating M789's fatigue performance in the presence of manufacturing (intrinsic) and artificially induced (extrinsic) discontinuities such as electrochemical pits, as the intended service environment predisposes the alloy to pitting corrosion. In contrast to Laliberté–Riverin et al. [20] that focused on testing only polished specimen, this work extends to as-printed and pitted specimens and constructs the Kitagawa-Takahashi diagram of the alloy using experimentally determined parameters. The predictive accuracy of the El-Haddad and Murakami models is then assessed by superimposing them on the experimental KT diagram, with the goal of identifying the discontinuity characteristics governing fatigue strength. This work provides the first experimentally validated assessment of discontinuity-controlled behaviour in LPBF M789 and is relevant to design methodologies for the use of the alloy in fatigue critical parts.

In this writing, a brief theoretical background is given in section 2, elucidating the development of the KT diagram along with the models of El-Hadad and Murakami. Then followed by the methodology in section 3, where the first part characterises the basic microstructure and mechanical properties of tensile, microhardness and the experimental determination of the $\Delta K_{th,LC}$. The second part focuses on the production of electrochemical pits on fatigue specimens. Also included in the section are the protocols adapted for the measurement, non-destructive characterisations, prediction of critical discontinuity size in the fatigue specimens, and the fatigue testing procedure. In section 4, the KT diagram is constructed using the experimentally obtained $\Delta K_{th,LC}$ and microhardness of the alloy. The models of El-Haddad and Murakami are also superimposed on the diagram. Next is section 5 presenting the prediction of the fatigue strength of the specimens using the discontinuity size from non-destructive characterisation. Sections 6 and 7 respectively focus on the results and discussion, and the conclusions reached are given in section 8.

2. Theoretical background

2.1. Effect of discontinuities on fatigue strength

The KT diagram describes the relationship between fatigue strength and discontinuity size by combining the discontinuity free strength with LEFM behaviour for long cracks [22]. The diagram (see Fig. 2) unveils regimes dominated by short and long cracks [23]. The fatigue strength for discontinuity-free material is expressed by Equation (1).

$$\sigma_a = \sigma_{w,0} \tag{1}$$

where $\sigma_{w,0}$ is the fatigue strength in MPa for stress ratio 'R' of −1 and can

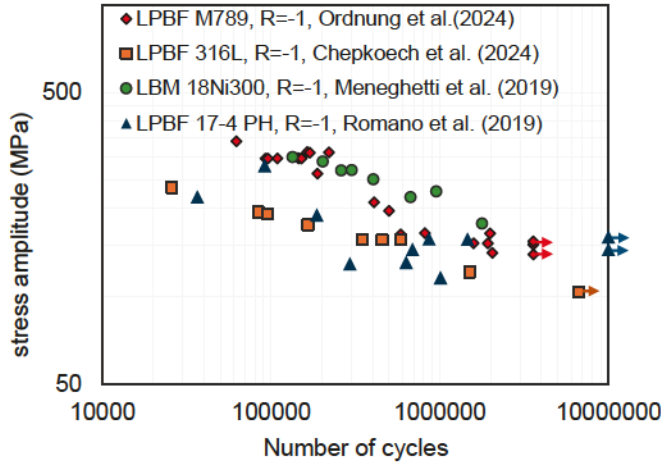

Fig. 1. Comparison of S-N data extracted from literature of axial fatigue of LPBF M789 [19], 316 L [54], 18Ni300 [55] and 17–4 PH [56].

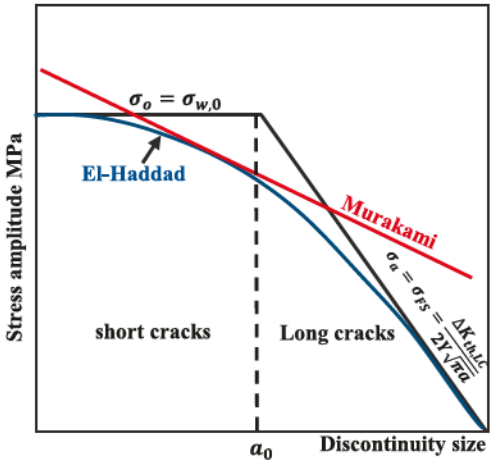

Fig. 2. A schematic representation of the Kitagawa-Takahashi diagram showing the evolution of fatigue strength with the size of discontinuity.

be estimated from the Vickers hardness (HV) using, $\sigma_{w,0} = 1.6\text{HV} \pm 0.1\text{HV}$, [24]. For components containing discontinuities, fatigue strength follows Equation (2).

$$\sigma_a = \sigma_{FS} = \frac{\Delta K_{th,LC}}{2Y\sqrt{\pi a}} \tag{2}$$

where $\Delta K_{th,LC}$ is the stress intensity threshold in MPa $\sqrt{m}$ for long cracks,a is the crack dimension in meters, σ_{FS} in MPa is the fatigue strength "Y" is a geometric correction.

2.1.1. El-Haddad's model of the KT diagram

Experimental results show a gradual transition between short and long crack behaviour. El–Haddad et al. [11] introduced a characteristic crack length (a_0) defined $a_0 = \frac{1}{\pi}\left(\frac{\Delta K_{th,LC}}{2\sigma_{w,0}}\right)^2$, to describe the transition by Equation (3).

$$\sigma_a = \sigma_{FS} = \frac{\Delta K_{th,LC}}{2Y\sqrt{\pi(a + a_0)}} \tag{3}$$

2.1.2. Murakami model of the KT diagram

Murakami [25] proposed $\sqrt{area}$ as a representative parameter for discontinuity size and derived a fatigue strength expression for materials containing small discontinuity [25] and the associated stress intensity factor given in Equation (4).

$$\sigma_{FS} = \frac{k(\text{HV} + 120)}{(\sqrt{area})^{1/6}} \tag{4}$$

where $\Delta\sigma$ is replaced with $2\,\sigma_{FS}$ in MPa, $k = 1.43$ and 1.56 for surface and internal discontinuities, and $\sqrt{area}$ in μm. For stress ratios (R) other than −1, Murakami [26] proposed correcting Equation (4) by the factor $\left[\frac{1-R}{2}\right]^{\alpha}$, where α is a material parameter given as

$$\alpha = 0.226 + \text{HV} \times 10^{-4}$$

From the discussions above, the El-Haddad (Equation (3) and Murakami (Equation (4) models show a reliance on discontinuity size ($\sqrt{area}$) and material property of microhardness and $\Delta K_{th,LC}$. These models inherently treat discontinuities as preexisting cracks to model the fatigue strength. Nonetheless, their modelling trend differs (as seen in Fig. 2) and can align differently with experimental results. The Murakami model leverages small discontinuities and does not explicitly cover long crack regimes. However, the El-Haddad model spans the regime of both short and long cracks, making it applicable from small to larger discontinuities. So, it is appropriate to ascertain which of the models is accurate for the newly developed LPBF-M789 alloy, which is likely to contain different discontinuity sizes before practical applications.

Terminology clarification: In this study, the term discontinuities is used uniformly to describe both intrinsic (manufacturing-related) and extrinsic (corrosion pits) features influencing fatigue behaviour. The term "defect'' appears only in the titles of cited references, where it reflects the authors' original terminology.

3. Materials and methods

3.1. Raw material and as-printed samples

Heat-treated M789 alloy specimens used for this research were produced by the voestalpine Additive Manufacturing Centre (vAMC), Mississauga, Ontario, Canada, using the LPBF AM process. Information on the feedstock powder and the building parameters employed during the LPBF build process for parts can be found in our previous work [20]. The chemical composition of the received alloy after part manufacturing is given in Table 1, where it is represented as "tested". Glow-discharge atomic emission spectroscopy was used for the measurement, while combustion analysis determined the carbon content. The results are compared to the patent specification of the alloy, where all the constituents except for Mn are in conformance. The Mn value is 0.05 wt%, which is less than the specified range of 0.50–1.50 wt%. Despite the out-of-specification value of Mn, the amount is considered to have no significant impact on this work. Though we note that Mn may be added to steel to favour the formation of MnS inclusions known to improve machinability, sometimes it is desired to be kept to a minimum to reduce the formation of inclusions [27].

Fig. 3a and b illustrate the layout of the build plate for the samples presented in Table 2. Cubic samples (pink) for metallographic observations and microhardness tests, two vertically built tensile samples (in red), two horizontally built tensile samples (indicated by green arrows) and fifteen fatigue samples (in yellow) were built vertically. Three rectangular bars (in purple) from the build plate in Fig. 3b are used to machine a single edge bending (SEB) specimen, used for crack growth threshold $\Delta K_{th,LC}$ characterisation. Other samples on the plate (grey, green, blue) were produced for parallel research projects and not presented in this paper. The dimensional drawings of the tensile and fatigue specimens are shown in Fig. 4 and Fig. 5, respectively.

3.2. Material characterisation

The results of material characterisation, excluding the fatigue behaviour, will be presented in the methodology since they are meant to provide general information about the tested material.

3.2.1. Microstructure

Specimens meant for microstructural characterisation were cut from the cubes using a Struers Secotom 20 machine, with cuts made in planes perpendicular (XY) and parallel (XZ) to the building direction. The extracted samples were mounted in phenolic resin and subjected to metallographic preparation. This involved sequential grinding with abrasive papers of 240, 400, 600, 800, and 1200 μm grits. Subsequently, the samples were polished employing diamond pastes with particle sizes of 6 μm, 3 μm, and 1 μm.

The polished specimens were etched using a modified Fry's reagent [28], composed of 1 g $CuCl_2$, 50 mL HCl, 150 mL H_2O, and 50 mL HNO_3. Etching was performed via sequential 10-second swabbing over a total duration of 140 s to prevent sample burning. After each swabbing step, the samples were rinsed with water and examined under an optical microscope. Fig. 6 presents the optical micrograph showing a random orientation of the martensitic microstructure with no visible melt pool tracks. This observation aligns with the work of Tian et al. [17], where no melt pool boundaries were visible in heat-treated M789 alloy samples. Discontinuities such as lack of fusion (LOF) and alumina non-metallic inclusions (NMI) were identified in the microstructure and

Table 1
Chemical composition of M789 alloy (in wt.%).

Elements	C	Mn	Cr	Mo	Ni	Cu	Ti	Al	Fe
Patent specification [16]	0.01–0.05	0.10–0.50	12.00–13.00	0.50–1.50	9.50–10.50	0.00–0.05	0.50–1.50	0.50–1.50	balance
Tested	<0.02	0.05	12.30	1.11	10.10	0.01	1.07	0.55	balance

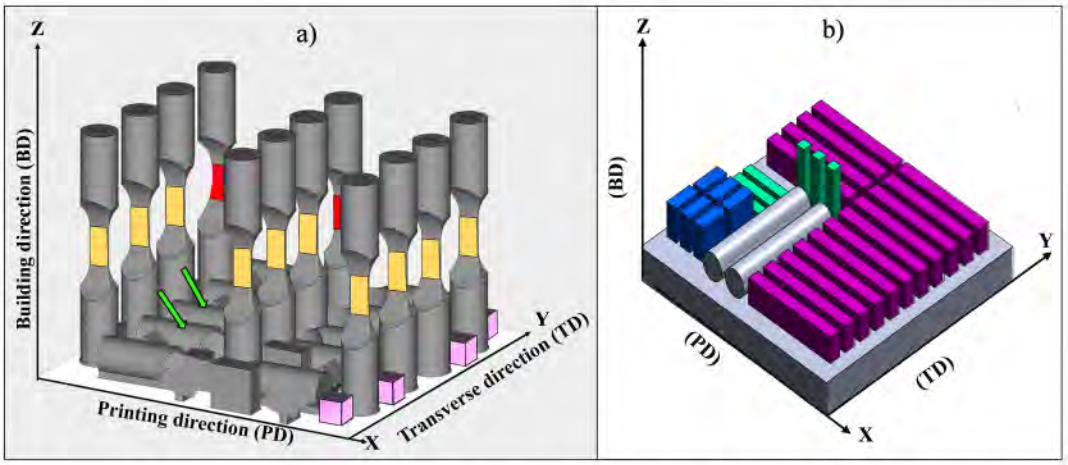

Fig. 3. Sample layout on build plates with reference guides for the M789 alloy, showing all specimens used in this work.

Table 2
Breakdown of samples used for this research, showing the dimensions, sample type, and quantity.

Sample	Dimension mm	Type	Number	Purpose
Cubic sample	17 x 17 x 17	NA Metallographic polishing	5	Microstructural characterisation and microhardness test
Tensile sample	Gauge 6 x 32 x 3	Vertical Horizontal	2 2	Tensile tests
Fatigue sample	Gauge 2.6 x 26 x 11.6	All vertical As-printed (FA) Polished (FP) Polished specimen then corroded (FC)	5 5 5	fatigue test
Rectangular bars	12.7 x 110 x 24	All vertical Polished	2	Estimation of $\Delta K_{th,LC}$ of the M789 alloy

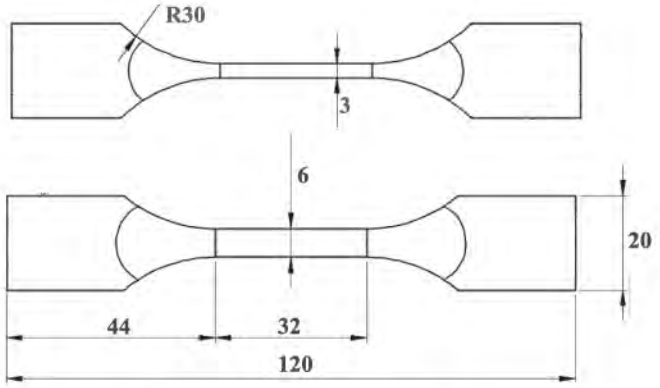

Fig. 4. Schematic representation of tensile specimen. All dimensions indicated are in mm.

are shown in Fig. 7. The acquired sizes of discontinuity using optical microscopy from both XY and XZ planes are plotted on a frequency distribution accompanied with cumulative distribution of plot of the exponential function in the secondary axis shown in Fig. 8. Across both planes, the measured discontinuity sizes predominantly ranged from 5 to 25 μm.

Revealing prior austenite grain boundaries (PAGBs) in quenched steels is often challenging, particularly in steels with low carbon content

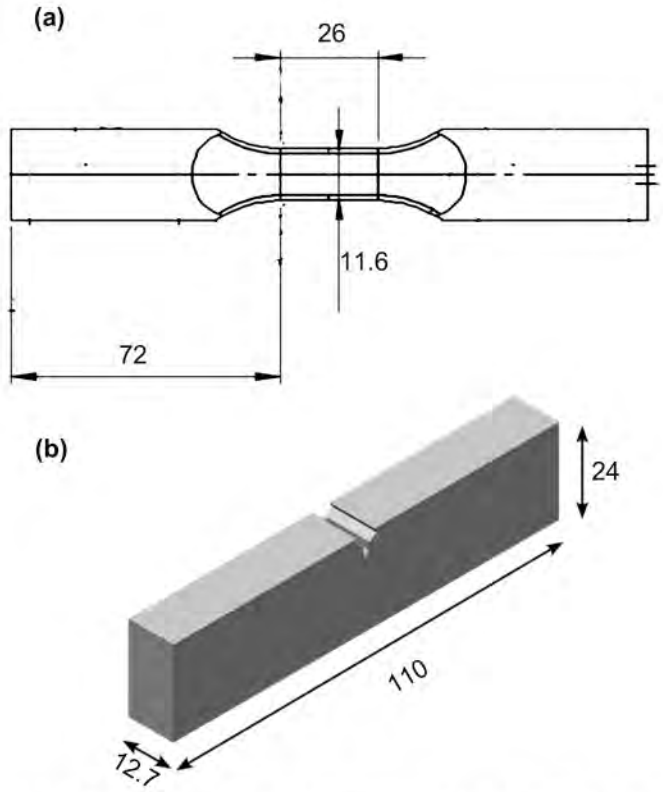

Fig. 5. Fatigue specimen: a) axial fatigue specimen, b) SEB specimen for stress intensity threshold test. All dimensions are in mm.

[24], and the M789 alloy proved no exception. This measurement was necessary to provide information on the size of the PAG, since it can contribute to the failure mechanism of the alloy. To address this, the oxidation method proposed by Faria et al. [25] was adapted. Metallographically prepared samples were austenitised at 750° C in a Pyradia electric furnace for 30 min. The samples were then air-quenched and lightly polished to remove the oxidised surface layer. They were then etched using Villela reagent, composed of 2 g picric acid, 5 mL HCl, and 100 mL ethanol. Austenitisation induced preferential oxidation along the austenite grain boundaries, creating topographic heterogeneities on the polished surface. Subsequent etching enhanced the optical contrast of these topographic grooves, allowing a distinction of the PAGB. The Keyence image analysis software was employed to observe and measure the parent austenite grain size (PAGS) in accordance with ASTM E112.

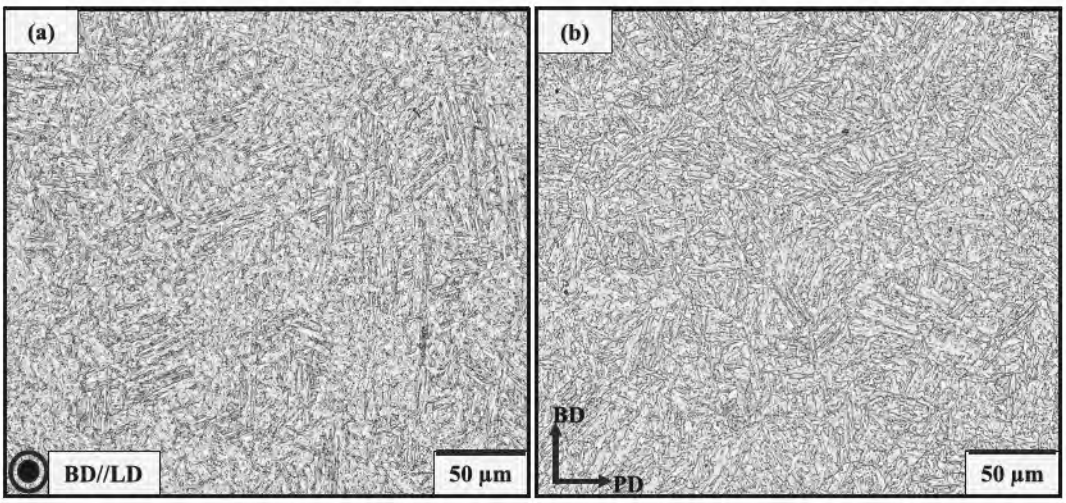

Fig. 6. Optical microscopic images of the M789 microstructure captured with the Keyence microscope: a) image of plane (XY) perpendicular to the BD, b) image of plane (ZX) parallel to the BD.

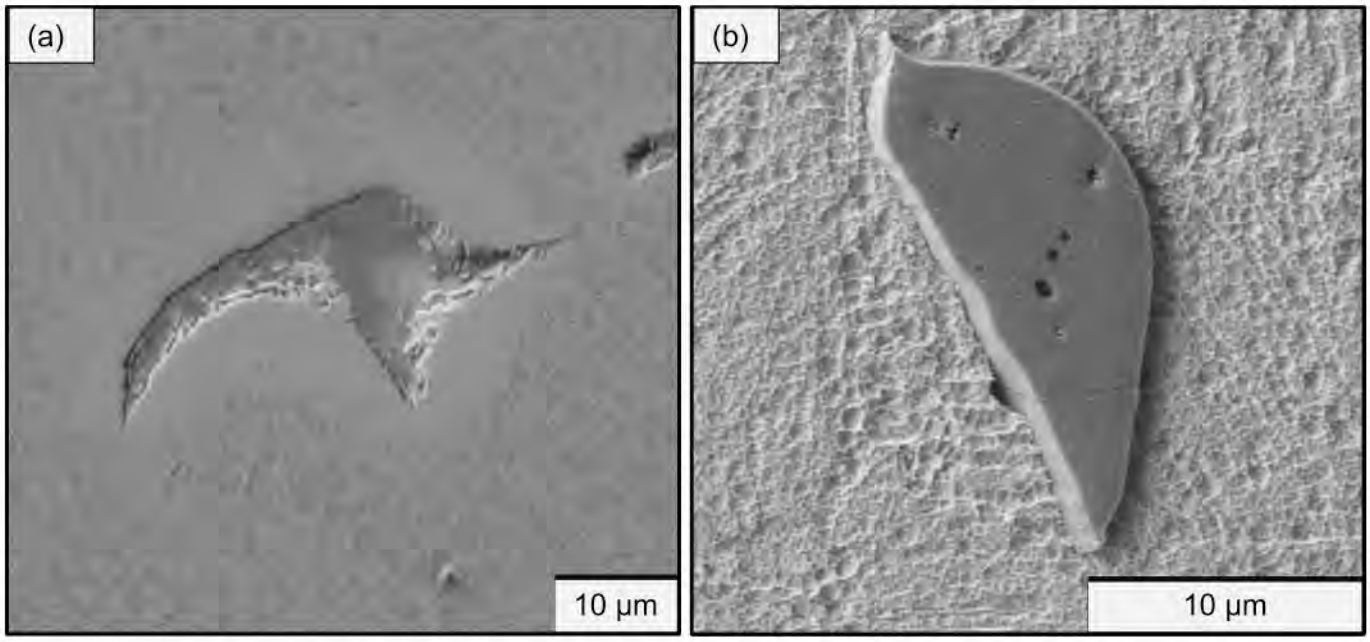

Fig. 7. Manufacturing discontinuities observed under SEM include a) LOF and b) alumina oxide non-metallic inclusion.

An example of the optical image generated with the traced out PAGs is shown in Fig. 9a, and the frequency plot of the equivalent circle diameter is shown in b. The PAG size ranged from 5 to 70 µm with an average of 22 ± 10.5 µm and an ASTM grain size number "G" of 6.8 ± 0.47. Notably, 90 % of the grains measured were less than 50 µm.

3.2.2. Tensile test

Four tensile tests were performed, two for each build orientation (horizontal and vertical) were performed according to ASTM E8/E8M [29] using a 100 kN servo-hydraulic machine at a nominal strain rate of 0.008 s^{-1}, with a 25.4 mm extensometer attached to the specimen. The tensile specimen had a rectangular gauge cross section measuring 6 × 3 mm and 32 mm gauge length, as shown in Fig. 4. The representative engineering stress–strain curves for each orientation from the test are presented in Fig. 10 and the others are provided in Fig. S1 of the supplementary information (SI). Similar tensile behaviours are seen irrespective of build orientation. The mean ultimate tensile strength and 0.2 % yield strength of vertically built specimens were 1800 MPa and 1685 MPa, respectively. Horizontally built specimens exhibited approximately 1.5 % higher ultimate tensile strength and less than 0.8 % higher yield strength. Additionally, the engineering strain to failure of horizontally built specimens was approximately 0.006 mm/mm higher than that of vertically built specimens. This difference is attributed to anisotropy inherent to LPBF alloys arising from discontinuities between build layers. Sarkar et al. [30] reported that vertically built LPBF specimens contain lack-of-fusion discontinuities, oriented perpendicular to the loading axis, promoting earlier strain localisation compared with horizontally built specimens, where discontinuities are more often aligned parallel to the loading axis. The present results are consistent with those reported by Tian et al. [18] and place M789 alloy within the class of high-strength steels as categorised by Li et al. [31].

3.2.3. Vickers microhardness test

Vicker's microhardness test was carried out in accordance with ASTM E384 using a BUEHLER Wilson VH1202 microhardness tester equipped with a diamond indenter. Measurements were performed on

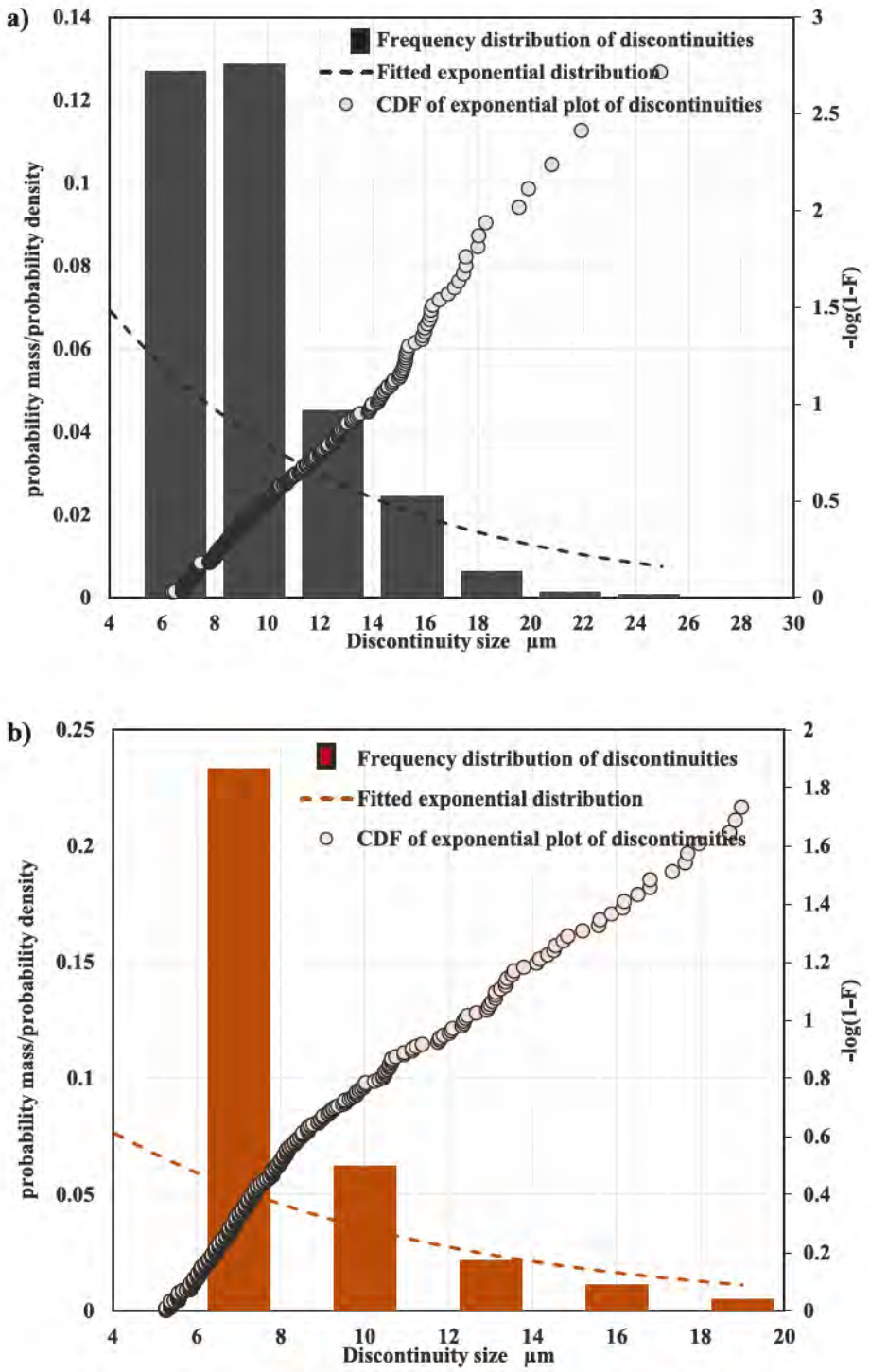

Fig. 8. Distribution of discontinuities acquired from cubic specimens showing frequency, fitted exponential distribution the cumulative distribution function (CDF) of discontinuities, of plane: a) XY perpendicular to the BD, b) ZX parallel to the BD.

polished transverse sections of cubic specimen. Prior to testing, the instrument's calibration was verified using a calibration reference test block. Indentations were made under a 0.5 kgf load with a dwell time of 10 s, and a total of 15 indents were placed with a minimum spacing of 2.5 times the diagonal length to avoid interaction effects. The average microhardness obtained from these measurements was 557 ± 11 HV.

3.3. Fatigue testing

3.3.1. Stress intensity threshold test

A single edge bending (SEB) specimen with dimensions shown in Fig. 5 was used for the crack propagation test. The fatigue testing process begins with finite element analysis (FEA) to estimate the appropriate load for pre-cracking. Using Abaqus software, the stress–strain behaviour of the material is incorporated into the model to simulate the plastic zone required to initiate a crack, as explained by Carboni et al. [29]. This precaution ensures precise control over crack formation while avoiding

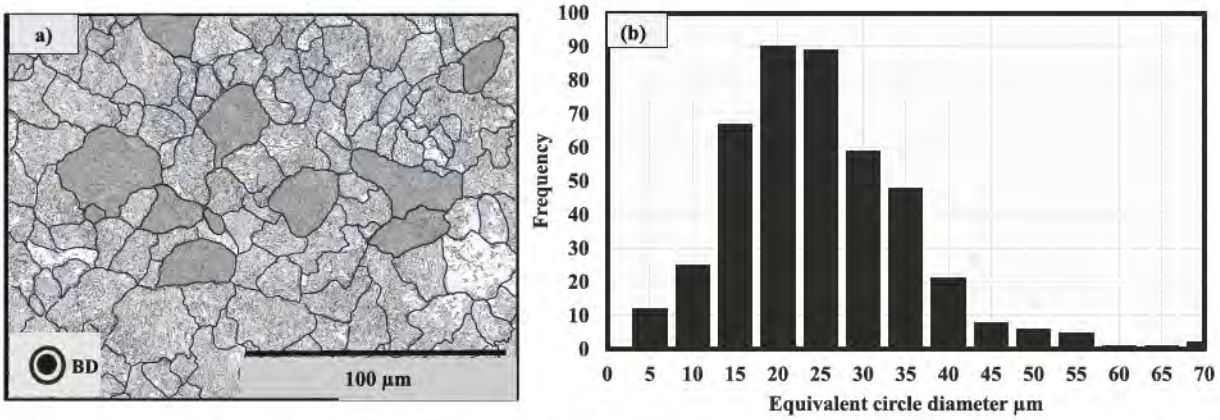

Fig. 9. Optical image of the PAGB after etching showing the grain boundaries in black, and b) frequency distribution of the measured PAGS.

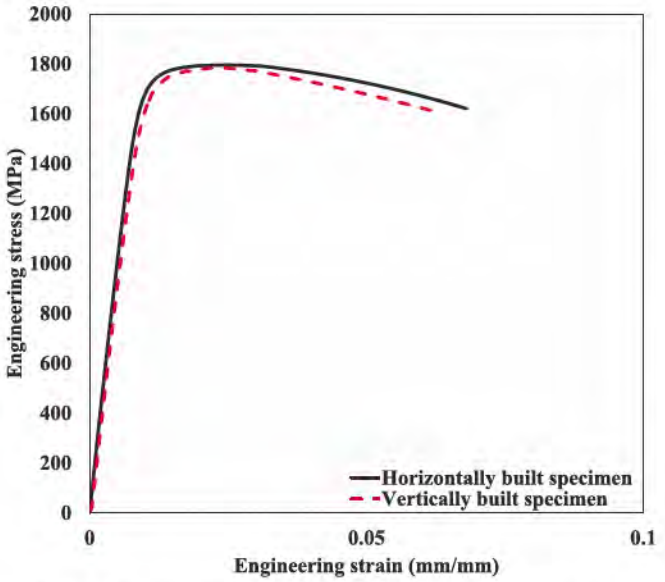

Fig. 10. Representative engineering stress–strain plot from tensile test.

unnecessary material damage. Once the load is determined, pre-cracking is performed using a compression-compression method. This approach prevents the formation of a plastic wake or residual stress that could influence subsequent crack propagation, as explained by Tabernig et al. [32]. The pre-crack is carefully grown to a size of approximately 100 µm, using a hydraulic testing machine for precise load control. Then, crack propagation testing is performed following the load reduction technique outlined in ASTM E647 [33] for an R-ratio of 0.1 and a shedding rate of -0.08 mm^{-1}. To accelerate testing without compromising accuracy, a resonant testing machine operating at around 105 Hz was used. The crack growth threshold ($\Delta K_{th,LC,R=0.1}$) was then determined from linear regression on near-threshold data. The regression used data points within the linear portion of the near-threshold regime for crack growth rates below 10^{-9} m/cycle, yielding a threshold value of 4.12 MPa $\sqrt{m}$ at 10^{-10} m/cycle. This value is smaller than the 4.42 MPa $\sqrt{m}$ theoretical estimate reported by Laliberte-Riverin et al [20]. The procedure is diagrammatically summarised in Fig. S2 of SI.

3.3.2. Constant amplitude fatigue testing

The fatigue testing protocol by Maxwell and Nicholas [34] was adopted to determine the fatigue strength of the material at a specified number of cycles. In this protocol, specimens are cyclically tested at constant stress amplitude starting from an initial stress amplitude ($\sigma_{a,o}$) lower than the estimated fatigue strength of the specimen for a given number of cycles N_{life}. If the specimen survives N_{life} cycles, the stress amplitude is increased by $\Delta\sigma_a$ and tested again. Each stress amplitude is called a step. The process is repeated n times, until failure occurs before or at N_{life}. Maxwell and Nicholas [34] proposed that once failure occurs, the material fatigue strength is characterised by the stress amplitude of the load step before failure $\sigma_{a,n-1}$, the load increment $\Delta\sigma_a$ and the number of cycles at failure N_{fail} using Equation (5). This methodology assumes that load steps anterior to $\sigma_{a,n-1}$ are not damaging the material.

$$\sigma_{FS} = \sigma_{w,\,Nlife} = \sigma_{a,n-1} + \Delta\sigma_a\left(\frac{N_{fail}}{N_{life}}\right) \tag{5}$$

where $\sigma_{w,Nlife}$ is the fatigue strength N_{life} cycles. This method has two merits: I) it is suitable for use where there is limited availability of samples, and ii) the fatigue strength at a desired number of cycles is determined for each specimen. Thompson et al. [35] conducted a study evaluating the step-loading technique for estimating fatigue strength in crankshaft-grade SAE alloys. They concluded that the method provides reliable fatigue-strength estimates and offers insight into the part's tolerance to discontinuities. Nevertheless, this fatigue testing approach can sometimes induce coaxing effects. In this study, such effects are assumed to be negligible because the alloy is a high-strength material, which typically exhibits limited plasticity and minimal cyclic strengthening. This assumption is supported by the findings of Nakajima et al. [36], who reported that coaxing effects diminish as material strength increases, with high-strength steels showing only minor or negligible improvements in fatigue resistance. Furthermore, preexisting intrinsic and extrinsic discontinuities are expected to dominate fatigue failure making it unlikely that prior low amplitude loading would significantly modify the fatigue response especially below the endurance limit. Under these conditions, any potential deviation introduced by step loading is expected to be small (on the order of a few percent, < 5 %).

This test procedure was applied to 15 fatigue test specimens having the dimensions reported in Fig. 5. Three different surface conditions were tested as reported in Table 2 and described in the next section. The fatigue tests were performed using a stress ratio of 0.1 on a servo-hydraulic machine equipped with a 100 kN load capacity. A frequency of 20 Hz, a target of $2{\cdot}10^6$ cycles at failure and a stress amplitude increment of 20 MPa were used. The choice of the number of cycles was selected to align with the high-cycle fatigue regime relevant to the intended application of the alloy, while providing reliable characterisation sufficiently beyond the low to high cycle transition region of the S-N curve. In addition, $2{\cdot}10^6$ cycles lie within the validity range of the Murakami model, defining the peak fatigue strength in the KT diagram [37]. Using a target of 10^7 cycles would significantly increase testing time without substantially altering the results of this study.

3.3.3. Selection of starting stress amplitude for the step loading protocol

A starting stress amplitude of 180 MPa was selected for the FP specimens based on the minimum fatigue strength reported for polished conditions in Laliberté–Riverin et al. [20]. As for the as-printed specimens (FA), no literature data were available at the time of testing, therefore, a starting amplitude of 100 MPa was used, guided by their predicted minimum fatigue strength given in Table 3 of section 5. For the pitted FC specimens, a starting stress amplitude of 60 MPa was chosen based on the predicted minimum fatigue strength associated with the largest measured pit size $\sqrt{area}_{max}$ also reported in Table 3. Collectively, these starting values were selected to ensure that all specimens began testing at stress levels below their expected fatigue strength and avoid premature failure.

3.4. Fractography protocol

After fatigue testing, a fractographic analysis of the failure surface for each specimen was conducted to identify and measure the discontinuity responsible for crack initiation. The fractured surface was separated from the specimen gauge section using the Struers secotom-20 machine for easy manipulation during the microscopic examinations. Each half of the fractured surface was sonicated in acetone with Branson 3800 equipment for 15 min to clean the surface of any organic material and impurities. The methodology used to measure the $\sqrt{area}$ of the discontinuities are presented in Fig. 11, showing 4 typical cases.

Case 1: tracing contours around the absolute shape of the discontinuity (LOF, NMI) found at the failure origin of polished or pitted specimens and computing the $\sqrt{area}$.

Case 2: tracing smooth contours to enclose the shape of the discontinuity (LOF, NMI) and its associated ligaments (a_1 and a_2) between it and the free surface. This applies to both polished and pitted specimens when the discontinuity is not open to the surface. The $\sqrt{area}$ is computed using Equation (6).

$$\sqrt{area} = \sqrt{area + a_1 + a_2} \tag{6}$$

Case 3: This case adopts the approach of Murakami [12], failures from closely situated discontinuities are considered as a single discontinuity if the distance of separation is less than the size of the smallest discontinuity. Applicable to polished and pitted specimens. The entire area in the red dashed line is used for the computation of the $\sqrt{area}$. This applies to the pitted specimen.

Case 4: failures from troughs for as-printed specimens measured by determining the depth of the trough found at the origin and treating it as a shallow, slender crack using the equation $\sqrt{area} = c\sqrt{10}$, where c is the depth.

Table 3
Summary of the results obtained from the NDC prediction of the fatigue strength (in amplitude) for FP, FA and FC specimens.

Specimen ID	Predicted $\sqrt{area}_{max}$ (μm)	Predicted fatigue strength (MPa)	Comment
FP01	56	219	Discontinuity measured on a metallographic specimen.
FP02			
FP03			
FP04			
FP05			
FA01	77	192	$\sqrt{area}$ predicted using $R_{V,max}$ of roughness values for each fatigue specimen. See section 3.5.2.
FA02	126	153	
FA03	122	155	
FA04	162	136	
FA05	96	173	
FC01	182	129	$\sqrt{area}$ measured from the largest pit on the pitted specimen.
FC02	372	91	
FC03	421	86	
FC04	221	117	
FC05	309	100	

3.5. Surface preparation and non-destructive characterisation (NDC)

3.5.1. Polished specimens (FP)

A hand rotating tool was used to polish the 4 surfaces in the gage length and fillet areas of 10 fatigue specimens. Special attention was given to rounding the edges, as crack initiation from these features can influence fatigue test results. Besides the tool used to polish, the polishing protocol described in section 3.2.1 was adopted. Five of these polished specimens were tested as-polished (FP), and the other five were submitted to the corrosion protocol described in section 3.5.3.

For the FP specimens, it is expected that the fatigue crack will initiate from natural discontinuities (internal or opened to the surface) such as LOF and NMI. Based on this assumption, the largest discontinuities observed during metallographic observation are critical. Ten regions, from the metallographically prepared cubic surface, each having an area of 20 mm^2, were inspected, and the $\sqrt{area}$ of the largest discontinuity in each region was recorded. An image of all the acquisitions is given in Fig. S4 of SI. The quantification was performed automatically under an optical microscope at a magnification of X200 using colour thresholding in-built image analysis software. These measurements will later be used in extreme value analysis (in section 5) for the prediction of the largest discontinuity expected to cause failure in the fatigue specimen.

3.5.2. As-printed specimens (FA)

For the FA specimens, no surface preparation was performed; they were used as manufactured. However, fatigue cracks are expected to initiate from surface roughness, either alone or in combination with microstructural discontinuities such as lack of fusion (LOF) or non-metallic inclusions (NMI). Therefore, surface roughness was characterised using an optical microscope with 3D reconstruction at 200 × magnification, a 1.5 μm height step, and auto-stitching to generate images of 1.4 mm × 1.1 mm per tile. To cover the entire gauge length, ten-line profiles, parallel to the loading direction (BD/Z axis), as shown in Fig. 12 (for FA01), were extracted from each as-printed fatigue specimen. In accordance with ASTM F3624 [38], a cutoff length of 2.5 mm was applied, and the maximum valley depth ($R_{v,max}$) was determined over five sampling lengths (SL#) for each line. By this protocol, ten $R_{v,max}$ is acquired for each FA specimen. The acquired $R_{v,max}$ values were transformed to $\sqrt{area}_{max}$ with the assumption of case 4 described in 3.4 where $C = R_{v,max}$.

3.5.3. Corroded specimens (FC)

Pits were introduced onto FP specimens using an in-house-designed electrochemical cell. A 1 cm^2 area on the specimen's gauge length was isolated for pitting using Gamry masking tape, after which the remaining region was coated using a 3 M electrical insulating sealer and left to dry for 15 min. Fig. 13a shows a coated fatigue specimen.

Subsequently, the specimen was affixed to the base of the electrochemical cell, sealed with a silicone coating (Fig. 10 b) and allowed to dry for 48 h. When dried thoroughly, the Gamry tape was carefully removed to expose the 1 cm^2 region. Next, the electrochemical cell was assembled and filled with the 3.5 % NaCl solution to a level sufficient to submerge the exposed surface (Fig. 13c). The solution was selected because it reliably promotes pitting corrosion and is widely used to simulate chloride-containing service environments in stainless steels, where chloride ions are known to destabilise passive films and initiate localised attack [39]. Furthermore, the alloy is intended for use as a die insert and involves liquid coolant circulation, which may introduce chlorides capable of inducing pitting, making this test solution representative of the in-service exposure. The resulting electrochemical setup consisted of the fatigue specimen (exposed surface in the electrolyte) acting as the working electrode (WE), a platinum wire as the counter electrode (CE), and an Ag/AgCl as the reference electrode (RE). Then, with a computer-controlled Biologic SP-150 potentiostat, a cyclic potentiodynamic polarisation (CPP) technique was employed to induce

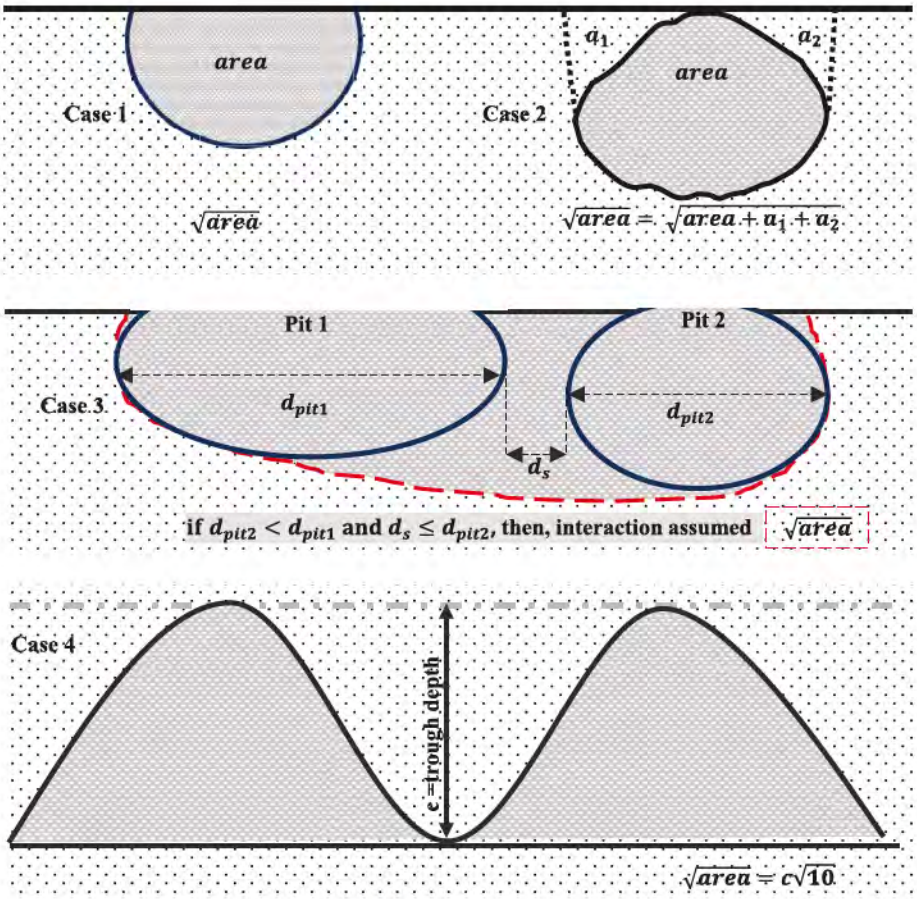

Fig. 11. Schematic description of discontinuity measurement protocols at the failure origin. Cases 1 and 2, surface and subsurface discontinuity at fracture origin. Case 3 closely situated discontinuities at the fracture origin. Case 4, failure from troughs of as-printed surfaces.

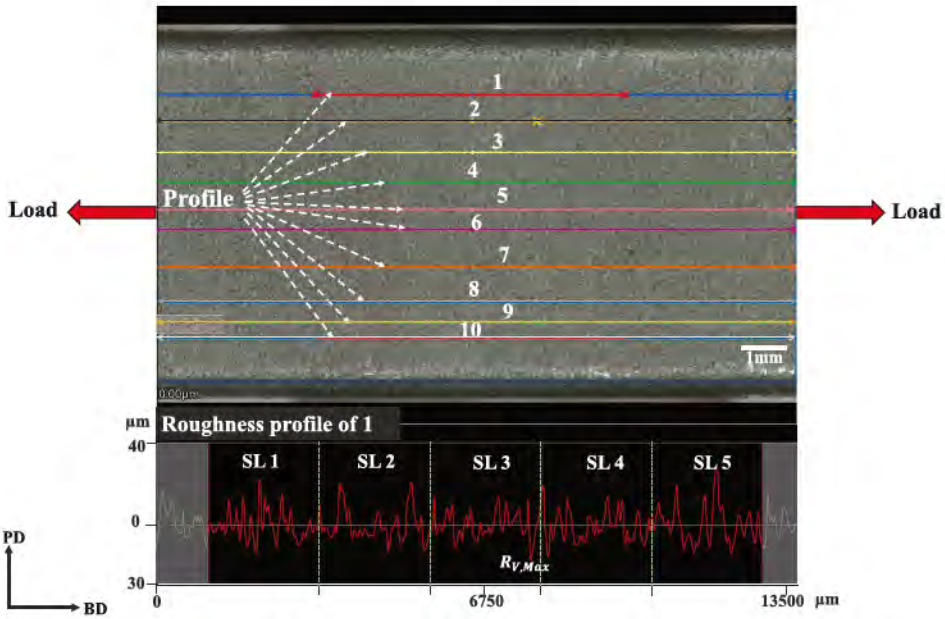

Fig. 12. Image of the acquisition of the roughness profile for specimen FA01.

pitting, using a scan rate of 0.167 mV/s within the range of −1 V to 1 V relative to the open circuit potential. The scan was allowed to complete automatically, and the resulting CPP plot is presented in Fig. S3 of the SI. The process was then repeated on another 1 cm^2 area of the specimen's surface. Five polished specimens were pitted using this technique.

The corrosion pits produced are anticipated to be the critical feature from which the fatigue crack will initiate. Therefore, the largest pit on each specimen was characterised using an optical microscope with 3D

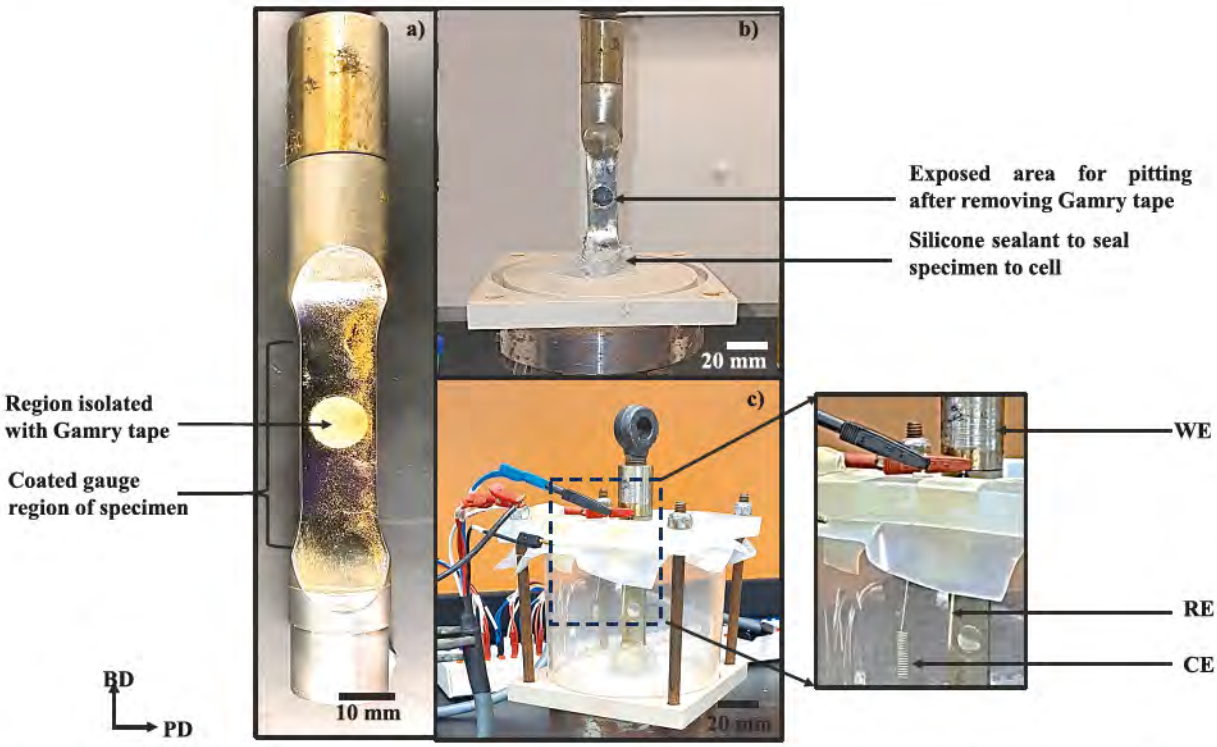

Fig. 13. A) coated specimen showing the isolated area b) specimen mounted on the electrochemical cell and sealed at the base using silicone c) coupled electrochemical cell showing the we, re and ce.

reconstruction capability to acquire the $\sqrt{area}_{max}$. An example of the two-step procedure is given in Fig. 14. Firstly, an inspection of the surface with the microscope is carried out to identify the largest pit, and a 3D reconstructed image of the pit is acquired. Fig. 14a shows the 3D image of the largest pit acquired with a depth composition with a step of 1.5 µm. Height colouration mapping helped to identify the deepest point (dark blue) of the pit, as labelled in the image. Then, a section line A-A cutting through the deepest point and perpendicular to the loading axis or BD of the specimen is used to help define the $\sqrt{area}$ critical to fatigue failure of the specimen. Fig. 14b shows a 2D representation with the sectioned line A-A (in black dashed line), the $\sqrt{area} = 421$ µm and pit depth is 224 µm. The process was repeated for all the corroded samples (FC01-FC05) and the $\sqrt{area}_{max}$ for each was acquired and reported in Table 3.

Representative images of the specimens after undergoing the surface preparations are shown in Fig. 15. The $\sqrt{area}_{max}$ of the discontinuity sizes acquired from the metallographic, as–printed (for specimen FA01) and the corroded specimen is shown in Fig. 16. A Gumbel's probability

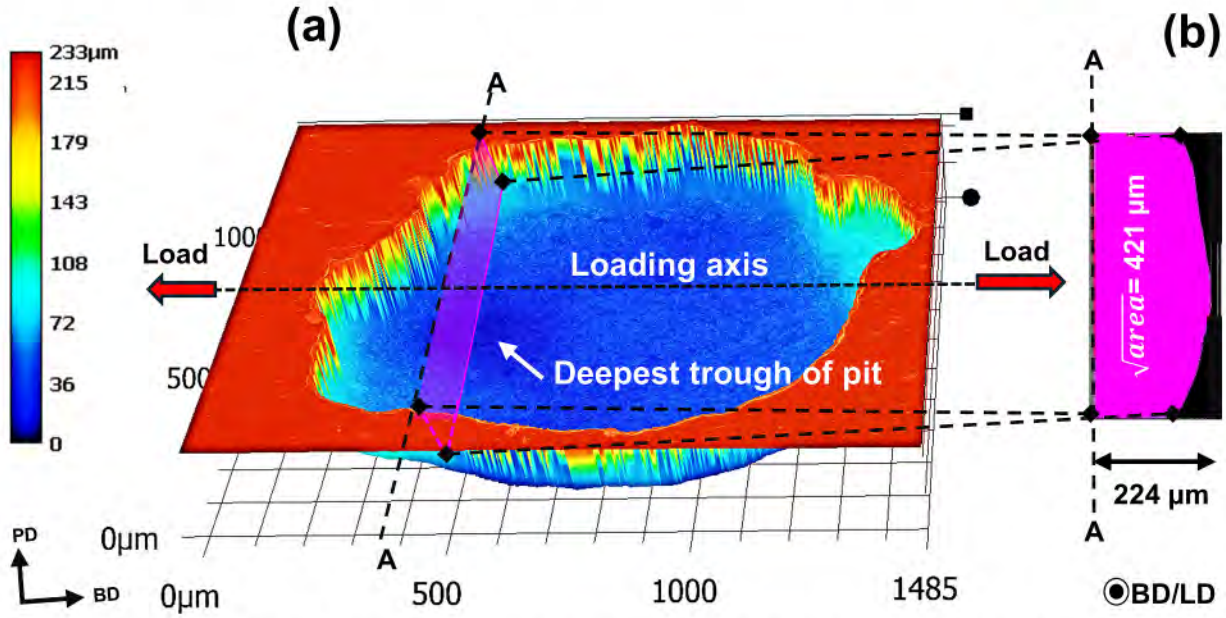

Fig. 14. Characterisation of severe pits using the Keyence microscope for specimen FC03. a) 3D colour mapping image of the largest pit b) 2D image of the characterised.

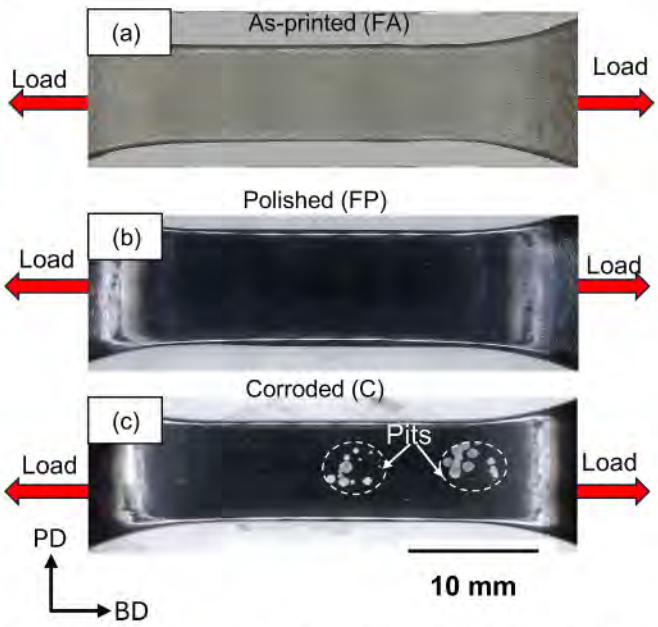

Fig. 15. Optical image of the Fatigue specimens after preparation, a) As-printed specimens (FA), b) polished specimens (FP), c) corroded specimens (FC) with pits as indicated by the white arrows.

density function (PDF) is fitted to the $\sqrt{area}_{max}$. From the diagram, the $\sqrt{area}_{max}$ of internal discontinuities in metallographic specimens ranged from 8 to 27 μm, which is less than the 47 to 62 μm of surface discontinuities estimated for the as-printed (FA01) specimen and the 182 to 409 μm for the corroded specimen (FC). Thus, with the size difference and surface condition, it can be anticipated that pits will most probably be the critical discontinuity across all specimens. These results demonstrate that testing the three different surface conditions allows studying a wider size range of discontinuities.

4. Generic KT diagram of M789 alloy

To construct the KT diagram of the M789 alloy for a stress ratio of 0.1 and $2{\cdot}10^6$ cycles, we require the fatigue strength of the alloy in the discontinuity-free or pristine state and the varying stress intensity threshold of the alloy $\Delta K_{th,LC}$. The values are respectively input to the models given by Equation (1) and (2), after which the plot type shown in Fig. 2 is generated for the alloy. The author has chosen to draw the KT diagram for a Y value of 0.65, which is associated with failure from the surface as estimated by Murakami [40]. This approach has been adopted because all the specimens failed from the surface, as will be seen in section 6, where the results are presented.

4.1. Fatigue strength of discontinuity-free or pristine M789 alloy

Laliberte-Riverin et al. [20] proposed a KT diagram for M789 using theoretical estimates of the $\Delta K_{th,LC}$ at $R = 0.1$. Here, we establish the diagram using experimentally obtained material properties of microhardness and the stress intensity threshold range at $R = 0.1$ ($\Delta K_{th,LC,R=0.1}$).

Firstly, the microhardness of the M789 alloy determined in section 3.2.3 is used to estimate the discontinuity-free fatigue strength "$\sigma_{w,0}$" which is calculated as 880 MPa using the relation $\sigma_{w,0} \cong 1.6\text{HV} \pm 0.1\text{HV}$ for $R = -1$. Thereafter, Goodman's [41] equation is used to estimate the fatigue strength, where S_u is the tensile strength and $R = 0.1$ as;

$$\sigma_{w,0.1} = \frac{1}{\frac{1}{\sigma_{w,0}} + \frac{1+R}{S_u(1-R)}} \tag{7}$$

The computed value of $\sigma_{w,0.1}$ was 550 MPa and is intrinsically related to the microstructure of the material in the absence of discontinuities. This value of $\sigma_{w,0.1}$ represent the horizontal line of the KT diagram.

4.2. The construction of the KTD of the M789 alloy

The $\Delta K_{th,LC,R=0.1}$ and $\sigma_{w,0.1}$ are employed to construct the KT diagram of the M789 alloy shown in Fig. 17. Also for comparison, the prediction models proposed by El-Haddad (Equation (3)) and Murakami (Equation (4)) are superimposed on the diagram. The value of the El-Haddad parameter $\left(a_0 = \frac{1}{\pi}\left(\frac{\Delta K_{th,LC}}{2Y\sigma_{w,0}}\right)^2\right)$ is 10.58 μm which is less than the 15.1 μm for the intersection point of LEFM and the Murakami model.

5. Fatigue strength prediction

To predict the fatigue strength, the largest discontinuity expected for each specimen condition was first estimated. The estimated

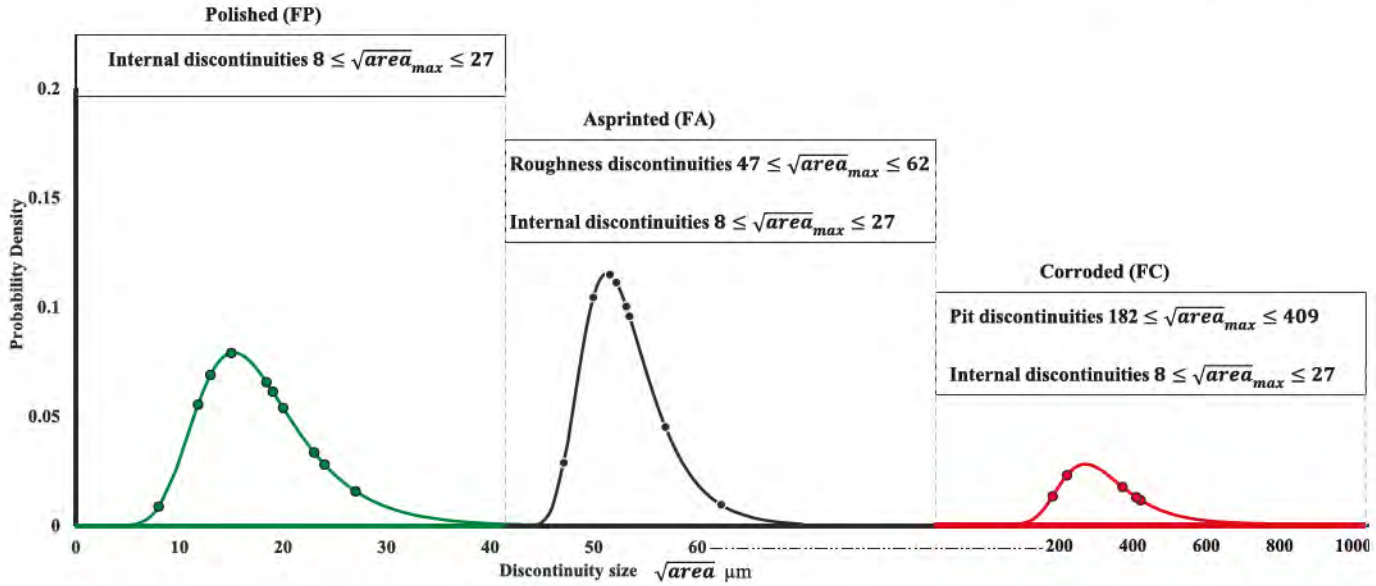

Fig. 16. PDF Gumbel fit discontinuity size comparison for as-printed, polished and corroded surface conditions.

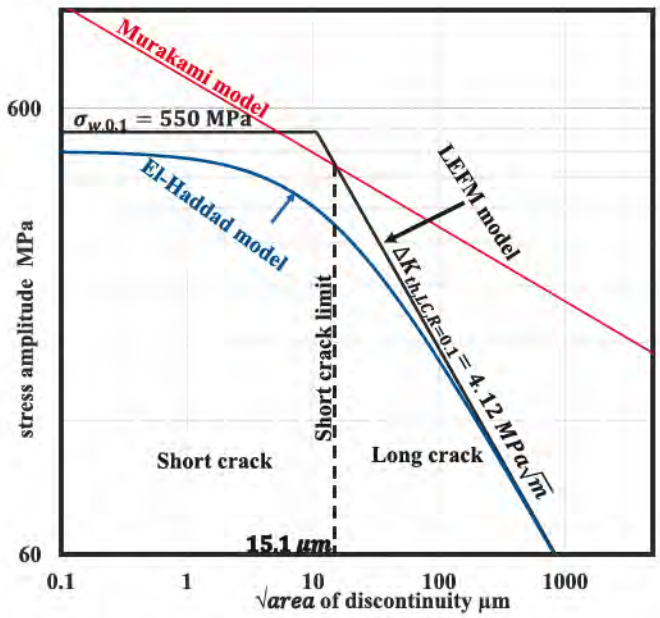

Fig. 17. The KTD of the M789 alloy constructed using experimental inputs of microhardness and $\Delta K_{th,LC}$ of the M789 alloy.

discontinuity size was then entered into the El–Haddad Equation (3) to obtain the predicted fatigue strength. The following subsection describes how the largest discontinuity was determined for each specimen condition.

5.1. FP specimens

Extreme value statistics (EVS) were applied to the measured $\sqrt{area}_{max}$ values of internal discontinuities obtained from the metallographic characterisation in section 3.5.1 to predict the largest expected discontinuity in FP specimens. The value obtained was then used to estimate the fatigue strength of the FP specimen. The inspection area A_0 = 20 mm^2 of the metallographic specimen is multiplied by the average size of the discontinuities to yield the inspection volume V_0 and the return period "T" is computed using Equation (8).

$$T = \frac{V_{ref}}{V_0} \tag{8}$$

Where V_{ref} is the fatigue specimen's gauge volume. The Maximum likelihood method, as described in ASTM E2283[42], is used to estimate the parameters of the EVS, and Equation (9) computes the expected largest discontinuity in the gauge volume of FP specimens.

$$\sqrt{area}_{max} = my + c \tag{9}$$

$$y = -ln\left(-ln\left(\frac{(T-1)}{T}\right)\right)$$

y is the reduced variate, m and c are the EVS distribution parameters, $\sqrt{area}_{max}$ is the expected largest discontinuity in the FP specimen, and T is the return period. A graphical illustration of the prediction of the EVS prediction is shown in Fig. 18. Only one prediction is performed for FP specimens using the metallographic data (Fig. S4 of SI). The scheme of the EVS has been detailed in our previous publication [20].

5.2. FA specimens

Similarly, for the FA specimens, EVS was applied to the measured $R_{v,max}$ values from the roughness characterisation in Section 3.5.2. The gauge section of the specimen served as the reference area "A_{ref}", while each profile multiplied by the average $R_{v,max}$ served as the inspection

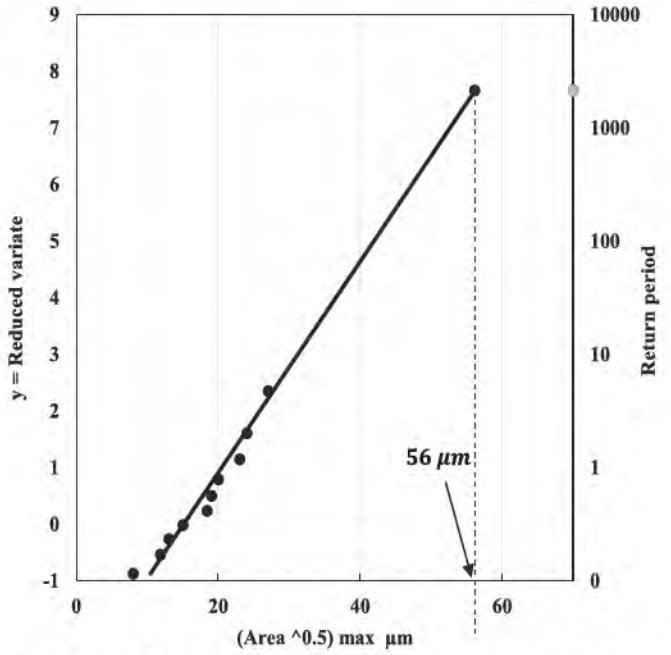

Fig. 18. Plot of EVS for the prediction of the expected largest $\sqrt{area}_{max}$ in FP specimen.

area A_0 used in the computation of T. The $R_{v,max}$ obtained from the prediction is subsequently used to estimate the $\sqrt{area}_{max}$ per Equation (10) Equation (10)

$$\sqrt{area} = R_{v,max}\sqrt{10} \tag{10}$$

A graphical illustration of the prediction for FA01, chosen as a representative, is shown in Fig. 19, and the remaining four are presented in the Fig. S4 of SI.

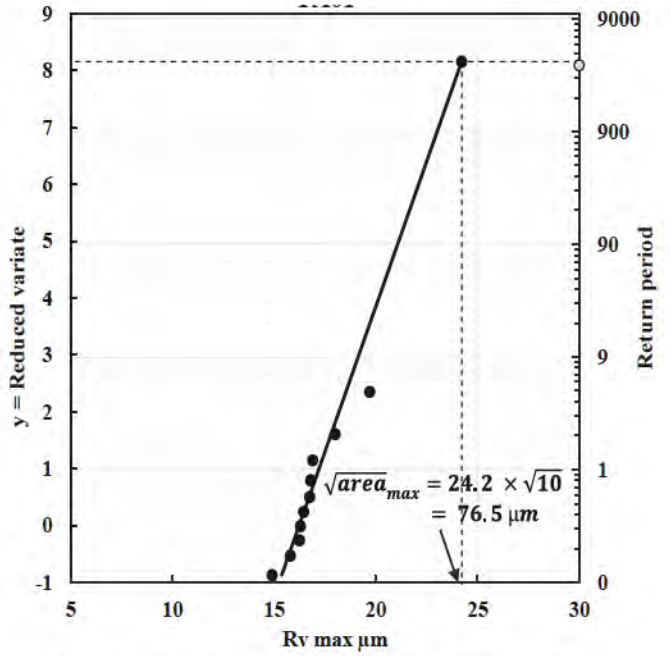

Fig. 19. Plot of EVS of the $R_{v\,max}$ values for the prediction of the expected largest $R_{v\,max}$ for specimen FA01. $R_{v\,max}$ is converted to..$\sqrt{area}$

5.3. FC specimens

In the case of the FC specimens, the computed $\sqrt{area}_{max}$ value from the characterisation of the largest pit on the corroded surface in section 3.5.3 was directly used to estimate the fatigue strength of each FC specimen.

Using the results of EVS predictions for FP and FA specimens and the characterised largest pits in FC specimens, the fatigue strengths were predicted using the El–Haddad model in Equation (3), and the results are reported in Table 3.

6. Results

6.1. Results of the fatigue test

The fatigue test results obtained using the step loading protocol are presented in Fig. 20 and reported in Table 4. The results show that the specimens experienced different numbers of steps before failure and this is attributed to the inherent fatigue scatter caused by variation in discontinuity size, geometry and distribution across the specimens. The results are rounded to the nearest whole number and ordered in increasing stress amplitude at failure for each specimen condition. All crack initiation sites observed are located at the surface (S) or subsurface (SS), irrespective of the surface condition. The last failure stress level for each specimen is reported in the $\sigma_{a,n-1}$ column and the number of cycles sustained at failure is reported in column N_{fail}. The computed fatigue strength using Equation (5) is reported in the 4th column. Representative images of the fractographic observation are presented in Fig. 22, and the discontinuity sizes are reported in the column of $\sqrt{area}$.

6.2. Fatigue performance of the M789 alloy

The fatigue performance of the M789 at 2.10^6 cycles with respect to the studied specimen groups (FA, FP and FC) is illustrated using the chart in Fig. 21. The coloured background bands represent different performance regimes relative to the peak fatigue strength (PFS) of 550 MPa determined in section 4.2. The diagram also includes the fatigue grade classification proposed by Murakami [43], which provides a common reference framework for interpreting fatigue performance in AM materials. None of the specimens was able to approach the peak fatigue strength of 550 MPa as they are all below the PFS. The FP specimens were the highest in performance (192 to 282 MPa), reaching the 30–70 % band of the PFS, hence spanning fatigue grades 2 and 3. In contrast, the respective fatigue strength of FA (122 to 165 MPa) and FC (103 to 226 MPa) specimens falls within the lower range of roughly 10–30 % of the PFS. Although we note that one FC specimen was in the 30–50 % band but it shall be discussed in section 7.1.4. Overall, the chart highlights the clear differences in fatigue performance among the three surface conditions of the alloy. The next section will focus on the observed discontinuities at the failure origin.

6.3. Fractography

Representative fractographic images of the discontinuities observed at the origin of FP and FA specimens are shown in Fig. 22.

The origins were characterised by the presence of either LOF (Fig. 22a) or NMI (Fig. 22b) situated at the surface, highlighted with the white dashed lines. NMIs accounted for the failure of 2/5 of the FP specimens with $\sqrt{area}$ of 44 to 51 µm. They exhibited irregular shape and have an alumina-based stoichiometry, as seen in the EDS result in Fig. 22c. The remaining failures were triggered by LOFs in the FP specimen, with a size range of 42 to 59 µm.

On the other hand, as-printed specimens failed from the surface asperities (troughs) as seen in Fig. 22d. The computed $\sqrt{area}$ using Equation (10) with 'c' as the trough depth ranged from 95 to 202 µm. The white arrowed line in Fig. 22d measures the depth (c) of the trough taken from the surface. The fatigue strength ranged from 122 to 165 MPa. Some as-printed specimens had crystallographic facets at the failure origin with $\sqrt{area}$ facet size range of 52–67 µm. Evidence of a facet-like feature (marked in white, broken dashed line) is seen beneath the trough in Fig. 22d. Other fractographic images showing facets are presented in Figs. S6–S8 of the SI. In Fig. 22e, the fractography show that the size of LOF, NMI and crystallographic facets are comparable in size to parent austenite grain sizes of 40–67 µm.

To unveil the underlying features of the LOF and provide an idea of its geometry, focused ion beam (FIB) milling was used to mill out 15 x

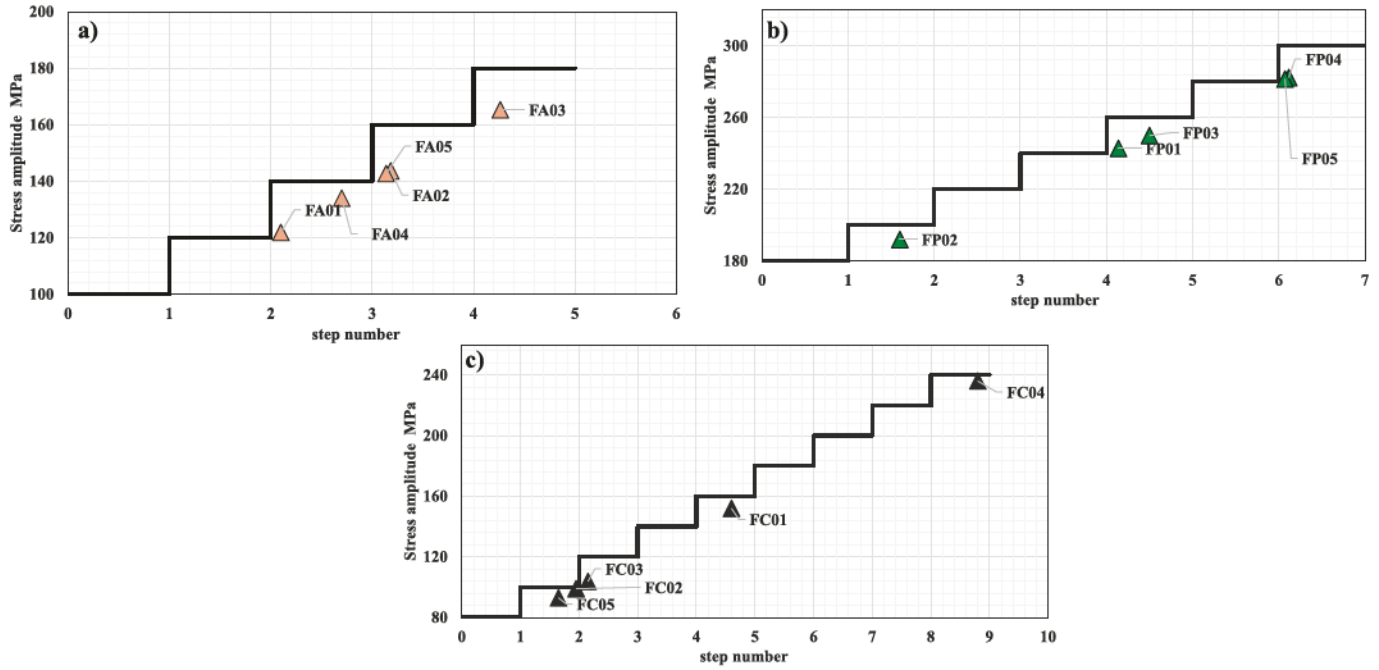

Fig. 20. Step loading protocol applied to the fatigue specimens showing the survived steps before failure. a) as–printed-FA specimens b) polished-FP specimens and c) corroded-FC specimens.

Table 4
Fatigue test results obtained for all specimens showing the computed fatigue strength, size type and location of discontinuities at the failure origin.

ID	$\sigma_{a,n-1}$ MPa	N_{fail}	$\sigma_{FS} = \sigma_{w,Nlife}$ MPa	$\sqrt{area}$ µm	Type of discontinuity	Location
FP02	180	$1.2.10^6$	192	59	LOF	SS
FP01	240	$2.0.10^5$	242	46	LOF	SS
FP03	240	$1.0.10^6$	250	51	NMI	SS
FP05	280	$1.0.10^5$	281	44	NMI	SS
FP04	280	$2.0.10^5$	282	42	LOF	SS
FA01	120	$2.0.10^5$	122	117	Trough	S
FA04	120	$1.4.10^6$	134	95	Trough	S
FA05	140	$3.0.10^5$	143	170	Trough	S
FA02	140	$4.0.10^5$	144	158	Trough	S
FA03	160	$5.0.10^5$	165	202	Trough	S
FC05	80	$1.3.10^6$	93	260	Pit	S
FC02	80	$1.9.10^6$	99	361	Pit	S
FC03	100	$3.0.10^5$	103	643	Pit (combined)	S
				465	Pit(isolated)	
FC01	140	$1.2.10^6$	152	123	LOF	SS
FC04	220	$1.6.10^6$	236	226	Pit	S

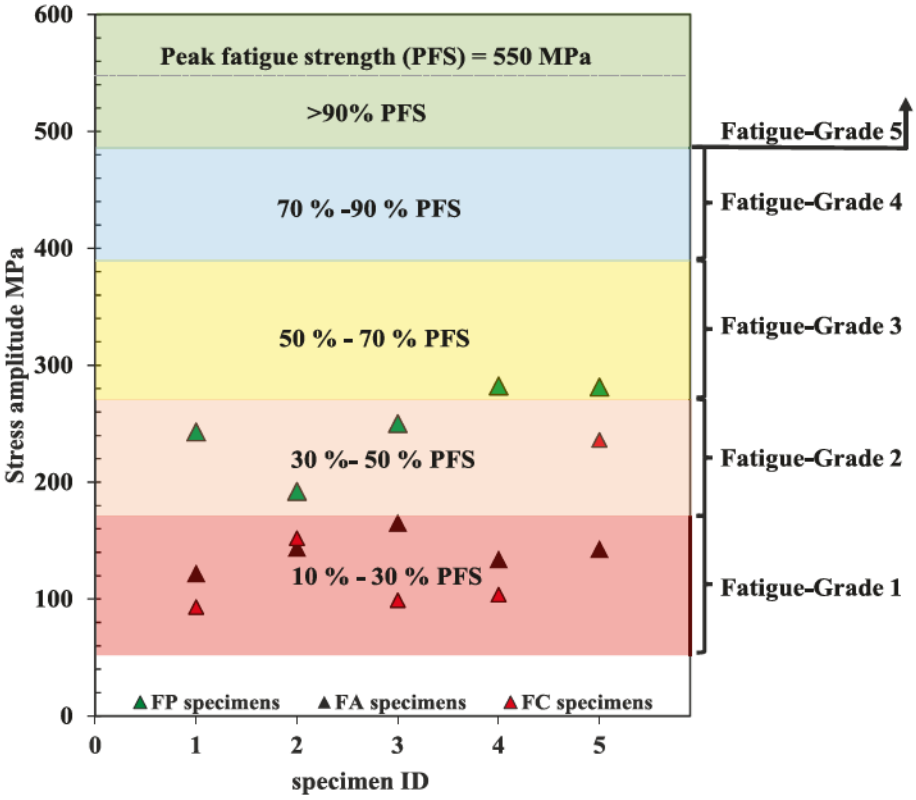

Fig. 21. Illustration of the fatigue performance of the group of specimens relative to the peak fatigue strength of the M789 alloy.

10 x 5 µm^3 material from the failure origin of one of the LOFs at the fractographic origin illustrated in Fig. 23. The LOF (Fig. 23a) marked in red dashed marks was milled on the X-X^1 section shown in Fig. 23b and c, while Fig. 23d is a magnified image of the milled region. The LOF exhibits a flat and irregular shape, while the FIB-milled region reveals the presence of interconnected subsurface LOF networks. These underlying micro-LOFs can contribute to the severity of the discontinuity causing failure.

The pitted specimens (FC) mostly failed from the pit, except for FC01, which failed from an LOF. Their fatigue strength ranged from 103 to 226 MPa, while the computed $\sqrt{area}$ of the pit at the failure site was in the range of 123 to 643 µm. The representative fractography shown in Fig. 24 for specimen FC03 reveals the existence of two pits (named Pit 1 and Pit 2) close to each other at the failure origin. The pits have an area of 376 µm and 465 µm, respectively. Murakami [12] proposes to calculate an overall area covering the pits and the connecting ligament when the distance (100 µm) between discontinuities is smaller than the size of the smallest discontinuity (376 µm). The application of this approach gives a discontinuity size of $\sqrt{area}$ = 643 um.

FC01 is an exception among the pit specimens as it failed from an LOF having $\sqrt{area}$ of 123 µm, despite the presence of an electrochemical pit of $\sqrt{area}$ 182 µm. Fig. 25a presents an optical image of the largest pit identified before fatigue testing. Fig. 25c and d show the specimen after failure, with the pit remaining unaffected and the fractographic origin marked by a lack of fusion (LOF) encircled in white dashed lines, respectively.

6.4. Presentation of the fatigue results on the KT diagram

The fatigue test data and the computed $\sqrt{area}$ of discontinuities at

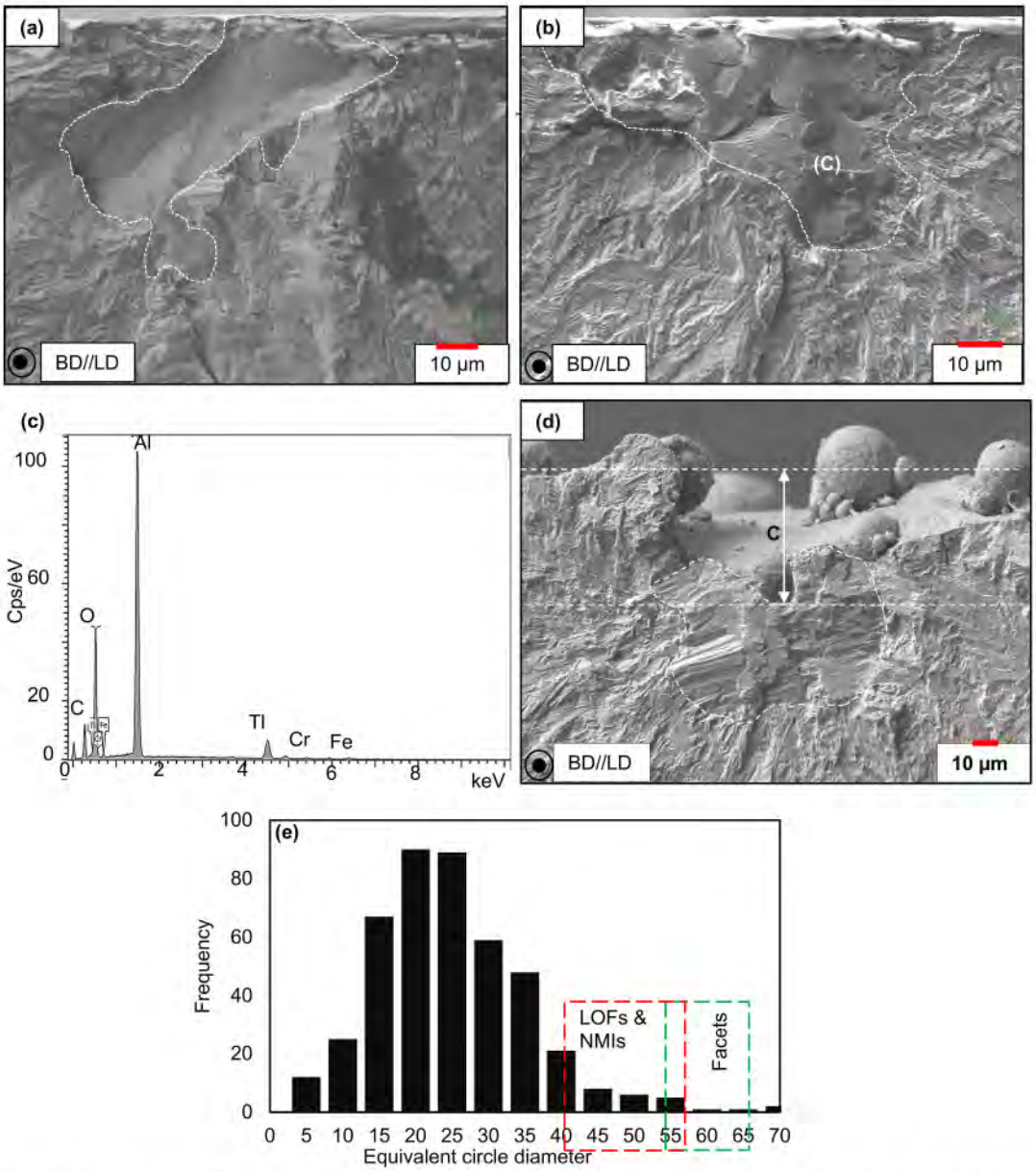

Fig. 22. Fractography showing a) LOF at the failure origin of FP01, b) NMI at the failure origin of FP02, c) The EDS results of the NMI in b, d) a failure from a trough from an as-printed surface for FA05, e) Size overlap of LOFs, NMI and facets on the PAGS.

the fracture origin of all specimens are presented on the KT diagram in Fig. 26.

Except for specimen FC04, the fatigue strength is well predicted by LEFM applicable to long cracks. The observed discontinuities range from 42 µm to 643 µm. For FC03, which failed due to two pits at the origin, its fatigue strength is represented using the combined (ligament-inclusive) $\sqrt{area}$ of both pits (red data point), as recommended by Murakami [12] and the $\sqrt{area}$ of the larger pit (brown data point). The use of the larger pits $\sqrt{area}$ (464.3 µm) yields a more precise prediction using LEFM, whereas using the Murakami's approach of combined $\sqrt{area}$ (643 µm) underestimated the fatigue strength. Notably, FC04 exhibits a fatigue strength higher than predicted by LEFM but lower than Murakami's estimate. Possible reasons for this behaviour are discussed in section 7.1.4.2.

6.5. Comparison between NDC predictions and fracture data

The comparison between the NDC characterisation (see Table 3) and experimental results (Table 4) for discontinuity size and fatigue strength is illustrated in Fig. 27a and b, respectively. The dashed 1:1 line represents perfect prediction accuracy, data above it indicates overprediction, and those below it indicates underprediction.

In Fig. 27a, for size comparison, overprediction corresponds to conservative estimates, while underprediction represents non-conservative ones. The results reveal a conservative trend for polished (FP) specimens, but non-conservative predictions for as-printed (FA) and pitted (FC). The average differences between predicted and experimental discontinuity sizes were 7.6 ± 6.8 µm (FP, conservative), −31.9 ± 59.0 µm (FA, non-conservative), and −32.3 ± 107.9 µm (FC, non-conservative). The negative sign denotes underprediction. The FC03 outlier skewed the FC's mean because of the assumed pit interaction (red data point in Fig. 27a). When this assumption is removed, and only the largest pit is considered (brown data point in Fig. 27a), the prediction becomes conservative with a mean difference of 3.3 ± 32.9 µm. Interestingly, the pit size for FC04 was accurately predicted despite appearing as an outlier in the KTD (see Fig. 26), suggesting that the fatigue

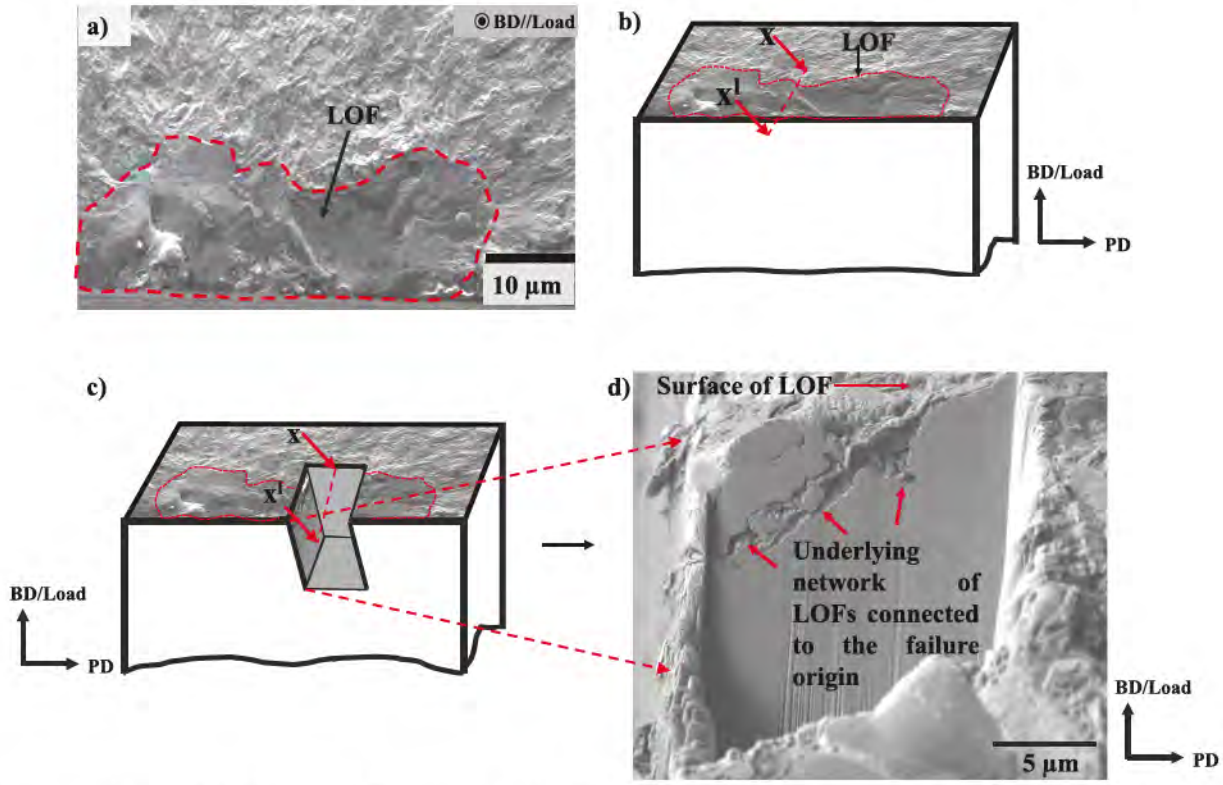

Fig. 23. A) fractographic image of lof b) schematic illustration of the identified section to be milled c) representation of the milled lof and d) region of milled lof showing the underlying lof network.

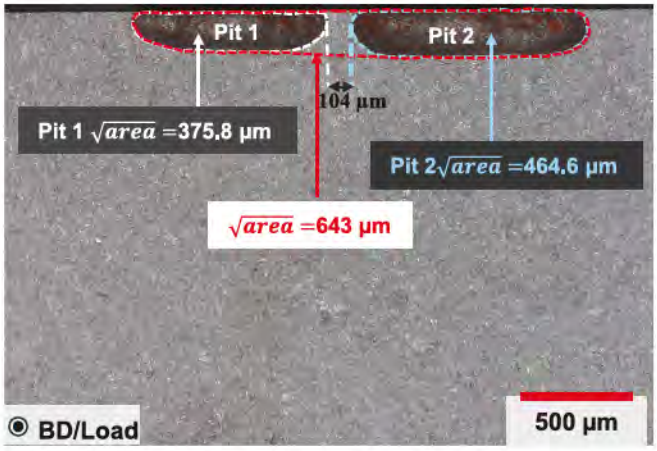

Fig. 24. Optical image of failure origin depicting failure from two closely situated pits at the failure origin of pitted specimen FC03.

resistance model lacked precision in estimating fatigue strength.

For fatigue strength Fig. 27b), points above the dashed line indicate unsafe predictions where predicted strengths exceed experimental results, while points below represent conservative predictions. Using the NDC and LEFM models together yielded safe predictions for eight out of fifteen specimens. Fatigue strength was generally underpredicted for FP and FC specimens and overpredicted for FA specimens. The average differences were −30.0 ± 36.8 MPa (FP, conservative), 20.0 ± 31.4 MPa (FA, non-conservative), and −32 ± 49.9 MPa (FC, conservative). This pattern aligns with the inverse relationship between fatigue strength and discontinuity size. Notably, although the discontinuity size of FC03 was underpredicted (due to neglecting proximity effects), its predicted fatigue strength (86 MPa) remained conservative compared to the experimental value (103 MPa). Similarly, for FC04, the experimental fatigue strength (236 MPa) was significantly higher than the predicted value (117 MPa), a point further discussed later.

7. Discussion of results

The fatigue test results unveil the scatter in fatigue strength for the LPBF-M789 alloy at 2.10^6 cycles across the different fatigue grades. The higher performance shown by the results (in Fig. 21) of the FP specimens reveals the benefit of the polishing on the fatigue performance. The FP specimens are of fatigue grade 2 to 3 zone, indicating a more than 48.7 % reduction from the PFS of 550 MPa. In contrast, that of the as–printed and pitted surface conditions are predominantly in the fatigue grade 1 classification, where the fatigue strength is between 10 and 30 % of the peak fatigue strength. It appears that even in the polished condition, the fatigue strength is unable to reach the PFS. However, the limited number of tested specimens and the specimen geometry constrain the range of discontinuity sizes observed at failure origins, which may influence the measured fatigue strength distribution. The result here, when compared to those in a recent work by Ordnung et al. [19] on the same M789 alloy, show similar trend despite using an incremental dual laser LPBF technology to improve the surface finish quality of the alloy. These findings reveal the limit of the peak fatigue performance of the M789 alloy in the polished condition at 2.10^6 cycles. The next sections focus on discussing the results, failure trigger discontinuities, failure mechanisms, and result comparison to the NDC predictions.

7.1. The discontinuities at the failure origins

The KTD presented in Fig. 26 reveals the evolution of the fatigue strength with the size of the discontinuities found at the failure origin for the tested specimens. Notably, because of the smooth surface finish, the polished specimens exhibited higher fatigue strength, ranging from 192 to 282 MPa, compared to that of the other specimen conditions, which

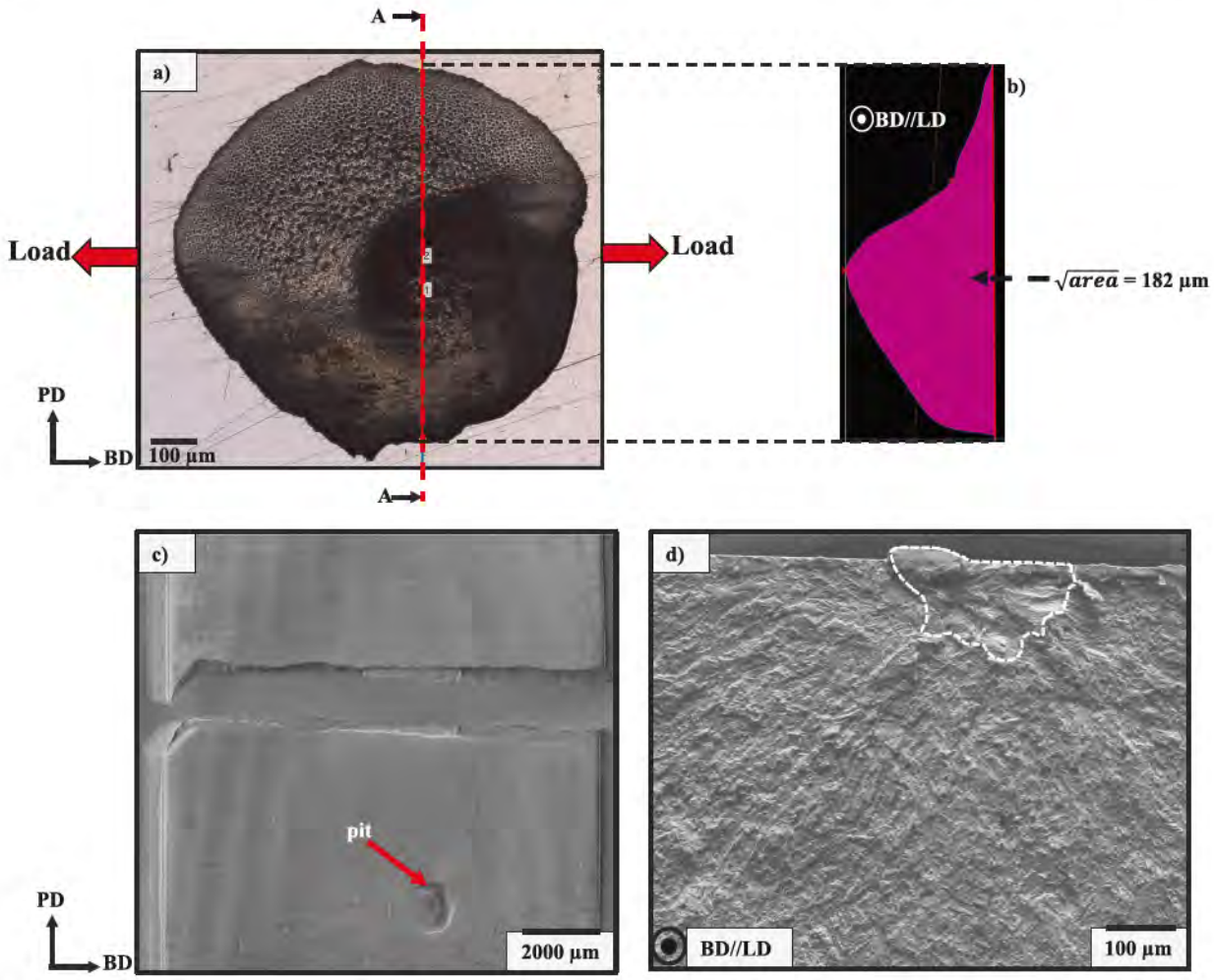

Fig. 25. Specimen FC01 with a) the most severe pit on the surface and b) section A-A of the pit, c) After fracture, optical image of the specimen with failure away from the pit, d) LOF discontinuity observed at the failure origin instead of the specimen.

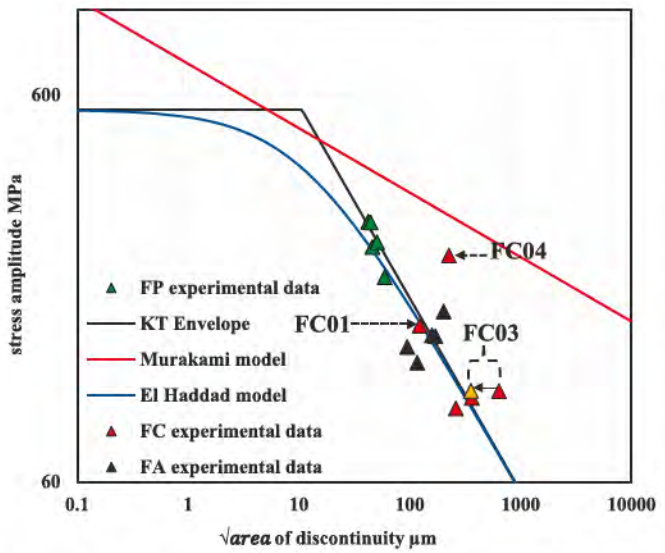

Fig. 26. The KT diagram of the M789 alloy with the superimposition of experimental data of all specimens.

ranged from 93 to 236 MPa. Complimentarily, polished specimens had the smallest discontinuities (42 to 59 µm), followed by the as printed (95 to 202 µm) and pitted (123 to 643 µm) specimens. These discontinuities are not necessarily the largest within the specimens (further explanation in 7.1.4.2), as one cannot rule out the presence of larger discontinuities capable of causing failure.

7.1.1. Failure mechanism of polished specimens (FP)

Naturally occurring discontinuities, particularly LOFs and NMI, were the main influencers of the fatigue strength of polished specimens of the alloy. The discontinuities showed no convergence towards any unique shape as they all exhibited different geometrical features, hence are deemed irregular. Their size range of 42 to 59 µm places them in the long-crack region of the KTD (Fig. 17), where the transition size between the Murakami model and LEFM is 15.1 µm. This positioning suggests a crack-like failure mechanism, with negligible cycles devoted to crack nucleation. The irregularity, especially with the alumina-based NMI, known for its brittle characteristics, enhanced the chances of intra-cracking and decohesion from the alloy's matrix, causing crack propagation.

7.1.2. Failure mechanism of as-printed specimens (FA)

As regards the as-printed specimens, their surface heterogeneity was critical to the fatigue strength. The range of the fatigue strength (122 to 165 MPa) for the as-printed specimens is smaller compared to that of the polished specimens (192 to 282 MPa) because of the rough surface. The presence of surface valleys and troughs, which are typical of LPBF alloys, often intensifies strain localisation under cyclic loading. This localised

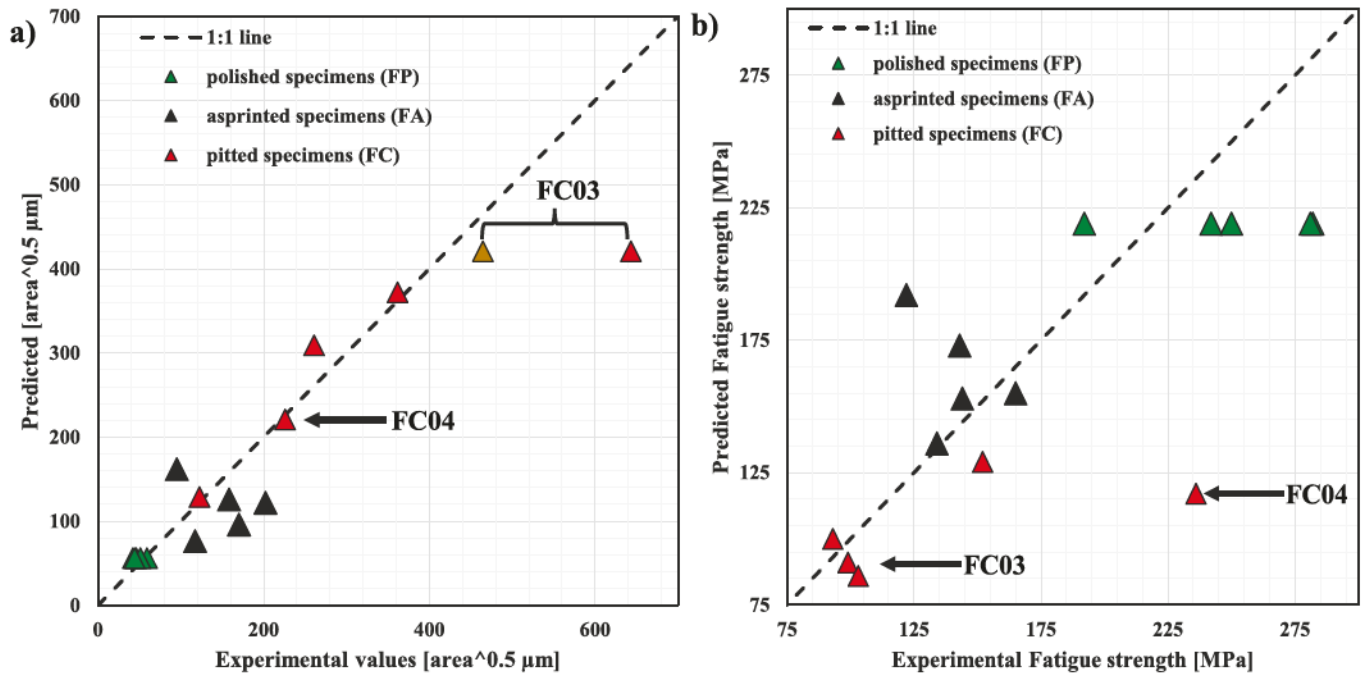

Fig. 27. Plot for comparison between predicted and experimental data: a) discontinuity size and b) Fatigue strength.

deformation, coupled in the highly stressed volume region, promotes a crystallographic failure mechanism evidenced by the presence of facets (see Fig. 22d of FA05) at the failure origin.

7.1.3. The short to long crack behaviour and the effect of microstructure

The behaviour of the alloy in the short crack region was not observed as the transition size of 15.1 µm (see Fig. 17) is smaller than the discontinuities measured at the failure origins. This made it challenging to validate the El-Haddad and Murakami models in the short crack regime, where microstructural influence is pronounced. One possible reason for this is the large size of the specimen's gauge volume, which biased failure towards larger discontinuities. A similar observation was reported in the work of Hu et al. [44] on LPBF-built Ti-6Al-4 V. They did not find intrinsic discontinuity sizes below 30–72 µm at the failure origin despite extensive testing. To trigger failure from smaller discontinuities, or the microstructure, would require a reduction of the specimen geometry or post-process operation like hot isostatic pressing (HIP). Masuo et al. [45], in their work on Ti-6Al-4 V alloy, have reported an improvement in fatigue strength of Ti-6Al-4 V alloy produced using electron beam melting. The improvement was to an extent of the fatigue grade 5 (peak fatigue strength), and it was attributed to the elimination and reduction in the size of discontinuities in the alloy realised through HIP. Another approach proposed by Pessard et al. [46] is to reduce the size of the highly stressed volume, which consequently reduces the likelihood of triggering larger size discontinuities. Accordingly, future work will focus on validating the El-Haddad and Murakami models in the short crack regime by modifying the highly stressed volume or, alternatively, using, smaller sized M789 specimens to promote crack initiation from microstructurally small discontinuities. In contrast, the El-Haddad and LEFM models were validated by the measured discontinuities at the failure origin and the associated fatigue strength, thereby unveiling their long crack-like behaviour.

Regarding the microstructure, the presence of crystallographic facets at the failure origin of some FA specimen hints at the influence of the hierarchical martensitic structure of the M789 alloy. Martensite typically exhibits a hierarchical structure in decreasing size order: PAG > packets > blocks > laths. Any of these substructure units can participate in the failure mechanism of the alloy and leave faceted features on the fracture surface [47]. In the case of martensitic stainless steels like the M789, cleavage facets are often associated with fracture along the (100) family of planes, which represent low atomic packing density and, consequently, the preferred cleavage path [48,49]. Facets are also linked to large preferentially orientated subsurface grains, which are weak microstructural links due to ease of slips and crack initiation. Kobayashi et al. [50] observed in their work that the size of the facet feature seen on the fracture surface of 718 alloy was consistent with large subsurface grains. As unveiled in Fig. 22, the facet sizes (62–69 µm), LOFs and NMI (42–59 µm) are comparable with the large PAGS (40–70 µm). Having such comparable sizes can breed a competition for crack initiation and propagation between the discontinuities and the microstructure. Although our results showed that cracks initiated from the discontinuities larger than the 15.1 µm theoretical long crack transition size, the microstructure influenced their subsequent propagation.

7.1.4. Failure mechanism of pitted specimens (FC)

The data of the electrochemically pitted specimens showed deviation from the long crack region of the KT diagram; important observations on the results of specimens FC01, FC03 and FC04 are discussed in the subsequent sections.

7.1.4.1. Competition between pits and LOF discontinuities. The competing effect between the pits and LOF discontinuity was seen in the result of specimen FC01. Despite the size of the pit with $\sqrt{area}$ of 182 µm on the specimen, the fatigue failure emerged from an LOF of a smaller size of 123 µm. The irregularity of the LOF likely enhanced its severity, making it more detrimental to the fatigue strength than the relatively smooth and regular pit (Fig. 25). The size difference between the two discontinuities (59 µm) was insufficient for the pit to control the fatigue strength of the specimen. This suggests the pit size in FC01 is not large enough to dominate the LOF discontinuity as the primary cause of failure. The observation is further supported by the prediction results (see Table 3), which show that the pit in FC01 is the smallest critical pit among all the FC specimens and was the only case where failure emanated from an internal LOF rather than a pit. It is also noteworthy that the size of the LOF discontinuity (123 µm) exceeds the estimated largest size of 56 µm from the EVS analysis of the metallographic specimen performed in section 5. This observation highlights the inherent stochastic nature of

discontinuities in the M789 alloy, which can account for deviations from analytical predictions and consequently alter the expected fatigue behaviour.

7.1.4.2. The interaction and shape effect of pits at the failure origin. The assumption of the interaction effect, consistent with Murakami's [12] view on fatigue strength, is particularly relevant for specimen FC03. This is because the smallest discontinuity (375 μm) exceeded the separation distance (104 μm), as shown in Fig. 24. Aman et al. [51] validated this interaction criterion when evaluating the influence of interacting small discontinuities on the fatigue limits of pure iron and bearing steel. This assumption of the pit interaction explains why FC03 appears as an outlier on the KTD plot (Fig. 26). Conversely, when interaction is not assumed, and only the largest pit of 465 μm is considered as the failure origin, the data align well (59 % improved accuracy) with the KTD in Fig. 26, suggesting that failure may have been governed by the largest discontinuity in isolation. The noninteraction assumption may be valid since M789, being a high-strength steel (HV > 400), exhibits low ductility and intuitively signifies a rapidly decaying stress field. Nonetheless, regardless of the assumption, the KTD trend remains conservative compared to the experimental results (Fig. 26).

For the shape, its influence is apparent on the fatigue strength of specimen FC04 (236 MPa, Fig. 26), which is about twice the value (117 MPa) predicted by the KTD. Depending on shape, a pit can behave either like a crack or a notch [47]. In the crack-like case, the fatigue strength is governed by the stress intensity factor (K) and a stress field exponent of 0.5, making it suitable for modelling with LEFM. Conversely, a notch-like geometry produces a lower stress field exponent (< 0.5), where fatigue strength is mainly influenced by stress concentration rather than K, making LEFM predictions conservative but less accurate (see Fig. 26). Fractographic analysis of specimen FC04 (Fig. S8 of SI) and finite element analysis (Fig. S9 of SI) returned a stress concentration factor k_t of 2.06 and a stress field exponent of 0.16 (see Fig. S10 of SI). Applying notch theory using k_t, the fatigue strength is expected to be the peak fatigue strength of 550 MPa divided by the k_t which gives 264 MPa. This value is closer to the 236 MPa obtained from the fatigue testing and is more accurate than the 117 MPa obtained using LEFM prediction. The pit geometry induced the notch-like behaviour, resulting in the higher fatigue strength observed in FC04. However, further targeted studies are needed to fully characterise the geometry-induced notch-like response of the alloy and to expatiate the influence of discontinuity proximity and interaction on the fatigue strength. These aspects will be explored in future work.

7.2. Disparity of NDC prediction from experimental data

In general, the NDC prediction and experimental data unveiled varying behaviour across the specimens. For the polished specimens (FP), EVS yielded conservative fatigue strength estimates, aligning well with predictions. This is not surprising, as many literature works have successfully applied it to internal discontinuities (LOFs and NMIs) to predict fatigue strength.

In contrast, the predictions of fatigue strength for the FA specimens were nonconservative, as the predicted sizes of failure discontinuity were smaller than what was observed on the fracture surfaces. One possible explanation for the variations is the complexity of the as-printed surface condition of the FA specimen. Features like surface profile, solidification cracks, overhanging powders and other discontinuities not considered can enhance the severity of the troughs and even trigger crystallographic failure mechanisms. Also, the contributing microstructural influence, as seen with the emergence of facets at the failure origin, cannot be understated. Hence, relying solely on trough depth for fatigue prediction in as-printed conditions may oversimplify the actual damage-driving mechanisms. However, it is worth mentioning that the use of EVS for as-printed surfaces yields a mixed bag of success stories in the literature. Nikfar et al. [52] recently applied the EVS to estimate the deepest valley of an as-printed Ti–6Al-4 V alloy and reported mean errors of 5–15 %. They, however, noted that the limited reliability of the approach may be attributed to quality control. The reader is also referred to the review of Beretta on 25 years of EVS for [53].

For the pitted specimens, using the largest surface discontinuity as the basis for fatigue predictions resulted in conservative estimates. However, deviations observed in the outlier data can be attributed to pit interactions or the absence thereof, as illustrated by specimen FC03. Additionally, the tendency of pits to follow notch theory contributes to the disparity with the predicted values. These outliers highlight the need for caution when relying solely on pit discontinuity size to estimate fatigue strength, particularly when the full geometry of the pit cannot be accessed during non-destructive characterisation due to its complex morphology.

8. Conclusions

This study examined the fatigue behaviour of recently developed LPBF-manufactured M789 alloy under polished, as-printed, and corroded surface conditions using a KT framework at 2.10^6 cycles. Based on the experimental, fractographic, and modelling analyses, the following conclusions are drawn:

I. Fatigue behaviour of LPBF M789 is governed by both manufacturing (intrinsic) and extrinsic discontinuities, with surface condition influencing performance levels corresponding to 50 % of peak fatigue strength for polished specimens and 10–30 % for as–printed and corroded specimens.
II. Fatigue strength of the alloy is well predicted by LEFM and El-Haddad models as manufacturing discontinuities have propagation behaviour comparable to long cracks, making the Murakami model unsuitable. In contrast, extrinsic discontinuities, such as corrosion pits adopt a notch behaviour.
III. Non-destructive characterisation and extreme value statistics provide conservative predictions of discontinuity size and the fatigue strength of the alloy for polished and pitted conditions but not for the as–printed.
IV. The alloy has limited sensitivity to interactions between neighbouring discontinuities, as fatigue strength predictions based on the largest discontinuity are 59 % more accurate than predictions using combined discontinuity sizes.
V. Microstructural features contribute to the alloy's failure mechanisms in the long-crack region, as crystallographic facet sizes at crack initiation sites are comparable to prior austenite grain sizes.

9. Declaration of generative AI and AI-assisted technologies in the manuscript preparation process

During the preparation of this work, the author(s) used [ChatGPT] to [Grammatical phrasing]. After using this tool/service, the author(s) reviewed and edited the content as needed and take(s) full responsibility for the content of the published article.

CRediT authorship contribution statement

K. Sanni: Writing – review & editing, Writing – original draft, Methodology, Investigation, Formal analysis, Conceptualization. **A. D'Andrea:** Writing – original draft, Investigation. **M. Cova:** Conceptualization. **L. Patriarca:** Writing – review & editing, Methodology. **M. Brochu:** Writing – review & editing, Supervision, Project administration, Funding acquisition, Conceptualization.

Declaration of competing interest

The authors declare that they have no known competing financial interests or personal relationships that could have appeared to influence the work reported in this paper.

Acknowledgements

The project was funded by the Natural Sciences and Engineering Research Council of Canada, NSERC (Application number 530064), Fonds de Recherche du Québec–Nature et Technologies, FRQNT, MITACS (Application number IT31224) and CRITM (Application number 2017-040), Quebec, QC, Canada.

We wish to acknowledge the financial, material, and scientific contributions of our partners, Sacmi Imola S. C (Imola, Bologna, Italy), and Hydro-Québec's Research Institute (Varennes, QC, Canada).

Finally, we thank voestalpine BÖHLER Edelstahl GmbH & Co KG (Kapfenberg, Austria) and voestalpine Additive Manufacturing (Mississauga, ON, Canada) for providing the printing powder and printing the parts.

Appendix A. Supplementary data

Supplementary data to this article can be found online at https://doi.org/10.1016/j.ijfatigue.2026.109627.

Data availability

Data will be made available on request.

References

[1] Gibson I, Rosen D W, Stucker B E, Additive manufacturing technologies : 3D printing, rapid prototyping, and direct digital manufacturing, 2015.
[2] Kan WH, Chiu LNS, Lim CVS, Zhu Y, Tian Y, Jiang D, et al. A critical review on the effects of process-induced porosity on the mechanical properties of alloys fabricated by laser powder bed fusion. J Mater Sci 2022;57:9818–65. https://doi.org/10.1007/s10853-022-06990-7.
[3] Widomski P, Kaszuba M, Dobras D, Terefinko D, Kołodziński M. Comparative study of different additive manufacturing methods for H13 tool steel. Materials 2025;18:5299. https://doi.org/10.3390/ma18235299.
[4] Wycisk E, Solbach A, Siddique S, Herzog D, Walther F, Emmelmann C. Effects of defects in laser additive manufactured Ti-6Al-4V on fatigue properties. Phys Procedia 2014;56:371–8. https://doi.org/10.1016/j.phpro.2014.08.120.
[5] Günther J, Krewerth D, Lippmann T, Leuders S, Tröster T, Weidner A, et al. Fatigue life of additively manufactured Ti–6Al–4V in the very high cycle fatigue regime. Int J Fatigue 2017;94:236–45. https://doi.org/10.1016/j.ijfatigue.2016.05.018.
[6] Chastand V, Quaegebeur P, Maia W, Charkaluk E. Comparative study of fatigue properties of Ti-6Al-4V specimens built by electron beam melting (EBM) and selective laser melting (SLM). Mater Charact 2018;143:76–81. https://doi.org/10.1016/j.matchar.2018.03.028.
[7] Nadot Y. Fatigue from defect: Influence of size, type, position, morphology and loading. Int J Fatigue 2022;154. https://doi.org/10.1016/j.ijfatigue.2021.106531.
[8] DebRoy T, Wei HL, Zuback JS, Mukherjee T, Elmer JW, Milewski JO, et al. Additive manufacturing of metallic components – Process, structure and properties. Prog Mater Sci 2018;92:112–224. https://doi.org/10.1016/j.pmatsci.2017.10.001.
[9] Nadot Y, Nadot-Martin C, Dragon A, Vincent M. Competition between surface defect and grain size under fatigue loading - ARMCO iron. Procedia Struct Integrity 2017;7:530–5. https://doi.org/10.1016/j.prostr.2017.11.122.
[10] Kitagawa H, Takahashi S. Applicability of fracture mechanics to very small cracks or the cracks in the early stage. In: editor(s). Proceedings of the Second International Conference on Mechanical Behaviour of Materials (ICM 2); Year; Cleveland, Ohio. ASM Metal Park; 627-631.
[11] El Haddad MH, Smith KN, Topper TH. Fatigue crack propagation of short cracks. J Eng Mater Technol 1979;101:42–6. https://doi.org/10.1115/1.3443647.
[12] Murakami Y. Effect of size and geometry of small defects on the fatigue limit. In: Metal Fatigue: Effects of small defects and nonmetallic Inclusions. London, United Kingdom: Academic Press; 2019. p. 39–59.
[13] Wu Z, Wu S, Bao J, Qian W, Karabal S, Sun W, et al. The effect of defect population on the anisotropic fatigue resistance of AlSi10Mg alloy fabricated by laser powder bed fusion. Int J Fatigue 2021;151:106317. https://doi.org/10.1016/j.ijfatigue.2021.106317.
[14] Cersullo N, Mardaras J, Emile P, Nickel K, Holzinger V, Hühne C. Effect of internal defects on the fatigue behavior of additive manufactured metal components: a comparison between Ti6Al4V and Inconel 718. Materials 2022;15. https://doi.org/10.3390/ma15196882.
[15] Bergant A, Marcos Soria R, Sergio Bustos I, Raúl Soul R, Hugo Yawny A, Alejandro. On the relative significance of roughness, printing defects and microstructure on the fatigue behavior of electron beam melted Ti-6Al-4V. Fatigue & Fracture of Engineering Materials & Structures 2025;48:1647–66. https://doi.org/10.1111/ffe.14565.
[16] Bohler MS. Method for the additive manufacturing of an object from a maraging steel powder. Patent number 2018. https://patents.google.com/patent/WO2019121879A1/en.
[17] Tian Y, Palad R, Aranas C. Microstructural evolution and mechanical properties of a newly designed steel fabricated by laser powder bed fusion. Addit Manuf 2020;36:101495. https://doi.org/10.1016/j.addma.2020.101495.
[18] Tian Y, Palad R, Jiang L, Dorin T, Chadha K, Aranas C. The effect of heat treatments on mechanical properties of M789 steel fabricated by laser powder bed fusion. J Alloy Compd 2021;885:161033. https://doi.org/10.1016/j.jallcom.2021.161033.
[19] Ordnung D, Mertens T, Tacq J, Nasab MH, Sinico M, Li G, et al. Enhancing fatigue life of as-printed martensitic M789 steel produced by laser powder bed fusion via in-process surface integrity improvement and phase change induced compressive residual stresses. Addit Manuf 2024;88:104263. https://doi.org/10.1016/j.addma.2024.104263.
[20] Laliberté-Riverin S, Yassine SR, Mena-Morcillo E, Sanni K, Cova M, Hassanipour M, et al. Microstructure, corrosion behavior, and fatigue resistance of laser powder bed fusion-produced precipitation-hardening martensitic M789 stainless steel. Surf Interfaces 2024;45:103830. https://doi.org/10.1016/j.surfin.2023.103830.
[21] Schonbauer BM, Mayer H. Effect of small defects on the fatigue strength of martensitic stainless steels. Int J Fatigue 2019;127:362–75. https://doi.org/10.1016/j.ijfatigue.2019.06.021.
[22] Kitagawa H, Takahashi S. Applicability of fracture mechanics to very small cracks or the cracks in teh early stage. In: editor(s). 2nd International conference on mechanical behaviour of materials-ICM2; Year; 627-631.
[23] Atzori B, Lazzarin P, Meneghetti G. A unified treatment of the mode I fatigue limit of components containing notches or defects. Int J Fract 2005;133:61–87. https://doi.org/10.1007/s10704-005-2183-0.
[24] Garwood MF, Zurburg HH, Erickson MA. Interpretation of tests and correlation with service: a series of four educational lectures on interpretation of tests and correlation with service presented to membres of the asm. American Soc for Metals 1951.
[25] Murakami Y, Endo M, Quantitative Evaluation of Fatigue Strength of Metals Containing Various Small Defects or Cracks, 17 (1983) 1–15. Doi: 10.1016/0013-7944(83)90018-8.
[26] Murakami Y. Martensitic stainless steels. In: Metal fatigue: effects of small defects and nonmetallic inclusions. United Kingdom: Academic Press; 2019. p. 432–50.
[27] Tanaka Y, Pahlevani F, Moon S-C, Dippenaar R, Sahajwalla V. In situ characterisation of MnS precipitation in high carbon steel. Sci Rep 2019;9:10096. https://doi.org/10.1038/s41598-019-46450-y.
[28] Author. ASTM E407-23: Standard Practice for Microetching Metals and Alloys. Standard No. ASTM, West Conshohocken, PA, 2023. https://www.astm.org/e0407-23.html.
[29] Carboni M, Patriarca L, Regazzi D. Determination of ΔKth by compression pre-cracking in a structural steel. J ASTM Int 2009;6:1–13. https://doi.org/10.1520/STP49292S.
[30] Sarkar S, Kumar CS, Nath AK. Investigation on the mode of failures and fatigue life of laser-based powder bed fusion produced stainless steel parts under variable amplitude loading conditions. Addit Manuf 2019;25:71–83. https://doi.org/10.1016/j.addma.2018.10.044.
[31] Li J, Zhan D, Jiang Z, Zhang H, Yang Y, Zhang Y. Progress on improving strength-toughness of ultra-high strength martensitic steels for aerospace applications: a review. J Mater Res Technol 2023;23:172–90. https://doi.org/10.1016/j.jmrt.2022.12.177.
[32] Tabernig B, Pippan R. Determination of the length dependence of the threshold for fatigue crack propagation. Eng Fract Mech 2002;69:899–907. https://doi.org/10.1016/S0013-7944(01)00129-1.
[33] Author. ASTM E647-24: Standard Test Method for Measurement of Fatigue Crack Growth Rates. Standard No., West Conshohocken, PA, 2024. https://www.astm.org/Standards/E647.htm.
[34] Maxwell DC, Nicholas T. A rapid method for generation of a haigh diagram for high cycle fatigue. West Conshohocken, PA: ASTM International; 1999. p. 626–41.
[35] Thompson T, Liu J, Hu C. A comparative analysis of step loading and staircase testing for fatigue strength estimation of an engine component. Fatigue & Fracture of Engineering Materials & Structures 2023;46:667–81. https://doi.org/10.1111/ffe.13898Digital Object Identifier (DOI).
[36] Nakajima M, Jung JW, Uematsu Y, Tokaji K. Coaxing effect in stainless steels and high-strength steels. In: Key Engineering Materials. Trans Tech Publications; 2007. p. 235–8.
[37] Murakami Y, Takagi T, Wada K, Matsunaga H. Essential structure of S–N curve: Prediction of fatigue life and fatigue limit of defective materials and nature of scatter. Int J Fatigue 2021;146:106138. https://doi.org/10.1016/j.ijfatigue.2020.106138.
[38] Author. ASTM F3624-23: Standard Guide for Additive Manufacturing of Metals – Powder Bed Fusion – Measurement and Characterization of Surface Texture. Standard No., West Conshohocken, PA, 2023. https://www.astm.org/f3624-23.html.
[39] Revie RW, Uhlig HH. Corrosion and corrosion control: an introduction to corrosion science and engineering. 4 ed. Hoboken, NJ: John Wiley & Sons; 2008.
[40] Murakami Y. Metal fatigue: effect of small defects and nonmetallic inclusions. 2nd Edition ed.,. Academic Press; 2019.

[41] Dowling NE. Mechanical behavior of materials: engineering methods for deformation, fracture, and fatigue. 4 ed. Upper Saddle River, NJ: Pearson Education; 2013.
[42] Author. ASTM E2283-19: Standard Practice for Extreme Value Analysis of Nonmetallic Inclusions in Steel and Other Microstructural Features. Standard No., West Conshohocken, PA, 2019. https://www.astm.org/e2283-08r19.html.
[43] Murakami Y, Masuo H, Tanaka Y, Nakatani M. Defect analysis for additively manufactured materials in fatigue from the viewpoint of quality control and statistics of extremes. Procedia Struct Integrity 2019;19:113–22. https://doi.org/10.1016/j.prostr.2019.12.014.
[44] Hu YN, Wu SC, Wu ZK, Zhong XL, Ahmed S, Karabal S, et al. A new approach to correlate the defect population with the fatigue life of selective laser melted Ti-6Al-4V alloy. Int J Fatigue 2020;136:105584. https://doi.org/10.1016/j.ijfatigue.2020.105584.
[45] Masuo H, Tanaka Y, Morokoshi S, Yagura H, Uchida T, Yamamoto Y, et al. Influence of defects, surface roughness and HIP on the fatigue strength of Ti-6Al-4V manufactured by additive manufacturing. Int J Fatigue 2018;117:163–79. https://doi.org/10.1016/j.ijfatigue.2018.07.020.
[46] Pessard E, Lavialle M, Laheurte P, Didier P, Brochu M. High-cycle fatigue behavior of a laser powder bed fusion additive manufactured Ti-6Al-4V titanium: effect of pores and tested volume size. Int J Fatigue 2021;149:106206. https://doi.org/10.1016/j.ijfatigue.2021.106206.
[47] Ševčík M, Hutař P, Zouhar M, Náhlík L. Numerical estimation of the fatigue crack front shape for a specimen with finite thickness. Int J Fatigue 2012;39:75–80. https://doi.org/10.1016/j.ijfatigue.2011.03.010.
[48] Morris J, Kinney C, Pytlewski K, Adachi Y. Microstructure and cleavage in lath martensitic steels. Sci Technol Adv Mater 2013;14:014208. https://doi.org/10.1088/1468-6996/14/1/014208.
[49] Pantazopoulos G. A short review on fracture mechanisms of mechanical components operated under industrial process conditions: fractographic analysis and selected prevention strategies. Metals 2019;9:148. https://doi.org/10.3390/met9020148.
[50] Kobayashi K, Yamaguchi M, Hayakawa M, Kimura M, Ogata T, Matsuoka S. High-cycle fatigue properties of alloy 718 for space use. J Jpn Inst Met 2004;8:523–5. https://doi.org/10.2320/jinstmet.68.523.
[51] Åman M, Wada K, Matsunaga H, Remes H, Marquis G. The influence of interacting small defects on the fatigue limits of a pure iron and a bearing steel. Int J Fatigue 2020;135:105560. https://doi.org/10.1016/j.ijfatigue.2020.105560.
[52] Nikfar M, Irfan S, Baugh L, Mahmood S, Ahmad N, Liu J, et al. On extreme value theory-based estimation of surface quality for metal additive manufacturing. Prog Addit Manuf 2025;10:6657–72. https://doi.org/10.1007/s40964-025-00998-6.
[53] Beretta S. More than 25 years of extreme value statistics for defects: Fundamentals, historical developments, recent applications. Int J Fatigue 2021;151:106407. https://doi.org/10.1016/j.ijfatigue.2021.106407.
[54] Chepkoech M, Omoniyi P, Owolabi G. Fatigue response of additive-manufactured 316L stainless steel. Metals 2024;14:988. https://doi.org/10.3390/met14090988.
[55] Meneghetti G, Rigon D, Gennari C. An analysis of defects influence on axial fatigue strength of maraging steel specimens produced by additive manufacturing. Int J Fatigue 2019;118:54–64. https://doi.org/10.1016/j.ijfatigue.2018.08.034.
[56] Romano S, Nezhadfar PD, Shamsaei N, Seifi M, Beretta S. High cycle fatigue behavior and life prediction for additively manufactured 17-4 PH stainless steel: effect of sub-surface porosity and surface roughness. Theor Appl Fract Mech 2020;106:102477. https://doi.org/10.1016/j.tafmec.2020.102477.